RUSSIAN ACADEMY OF SCIENCES
SIBERIAN BRANCH
LAVRENTYEV INSTITUTE OF HYDRODYNAMICS

DMITRI ALEXANDROVICH MEDVEDEV

SIMULATION OF HYDRODYNAMIC AND ELECTROHYDRODYNAMIC FLOWS BY LATTICE METHODS

PhD Thesis

Supervisors:
PhD A.L. Kupershtokh
Prof., Dr. Sci. A.P. Ershov

Novosibirsk – 2002

Contents

INTRODUCTION **4**

1 Lattice methods in fluid dynamics **8**
1.1 Lattice gas method 8
1.2 Lattice Boltzmann equation method 12
1.3 Simulation of thermohydrodynamic flows 15
1.3.1 Connection between the LBE method and differential equations 16
1.4 Simulation of multiphase and multicomponent flows 17
1.5 Transport of passive scalar 20
1.6 Use of the LBE method to solve parabolic and elliptic PDEs . . 20

2 Simulation of convective detonation waves in a porous medium **22**
2.1 Discrete model of convective wave 23
2.2 Computation results 26
2.3 Effect of heat losses 28
Summary 32

3 Simulation of mixing of heterogeneous HE components **33**
3.1 Diffusion 34
3.2 Small-scale instabilities 35
3.3 Flow around the cylinder 35
3.4 Effect of the initial system geometry 38
3.5 Mixing due to the pulse acceleration 41
3.6 Computation of the electric conductivity 41
Summary 45

4 Simulation of electrohydrodynamic flows **46**
4.1 Computation of charge transport 47
4.1.1 Convective charge transport 47
4.1.2 Conductivity currents 50

4.2 Electrodynamic forces 50
4.3 Two-dimensional EHD flow (EHD-pump) 51
4.4 Generation of vapor bubbles at the electrode surface in high electric field 54
Summary 56

5 Structure and dynamics of "plasma" channels at the electric breakdown of dielectric liquids 58
5.1 Streamer propagation in dielectric liquid 58
5.2 Channel stage of the electric discharge in liquid 59
5.3 Model of the transition layer 62
Summary 63

CONCLUSIONS 64

INTRODUCTION

This work deals with the study of fluid flows in different hydrodynamic and electrohydrodynamic processes (detonation waves in a porous medium, mixing of detonation products, inception and development of the electric breakdown in liquids), and related instabilities. Fluid flows are simulated by the lattice gas and lattice Boltzmann equation methods, that are relatively new methods based on the solution of the kinetic equation for simple model system.

Macroscopic dynamics of fluid is the average result of motion of its individual molecules. Interaction between molecules specify the properties of substance. Thus, one can simulate the behaviour of interacting particles itself and obtain macroscopic quantities (density, mass velocity, pressure and temperature) by averaging. This approach underlies the molecular dynamics method. In this case, the discretization of a problem (individual particles) corresponds to the properties of real physical world. The number of molecules in virtually any real system is so great that the full-scale simulation is most likely impossible ("one needs a gram-molecule of computers in order to simulate a gram-molecule of substance"). Therefore, one have to restrict oneself to comparatively small systems with further extrapolation of the results obtained to much larger spatial and temporal scales.

The approach of traditional hydrodynamics is, on the contrary, essentially macroscopic. The numerical methods consist of the solution of partial differential equations discretized properly in space and time. The variables in this case are macroscopic quantities themselves.

Lattice methods lie in a sense between micro- and macroscopic approaches. One can name them mesoscopic. The theoretical basis of lattice methods is the fact, that macroscopic behaviour of a medium only slightly depends on the details of its microscopic structure. The particularities of the structure and interaction of particles affects only the transport coefficients (diffusivity, viscosity and heat conductivity). One can therefore choose very simple microscopic properties (that should significantly simplify the computations), and hope nevertheless to obtain on the macroscopic level an adequate description of real medium.

Lattice methods have common features both with the molecular dynamics (the dynamics of system of particles are considered, although they have extremely simple properties) and with the usual finite-difference methods (the space and time are discretized too).

Of course, there are no ideal computation method, each approach has advantages on a certain class of problems. Lattice methods are superior in the

computation of flows where the structure and interaction on a mesoscopic scale are essential. The simulation of such flows is a subject of this work.

Dissertation consists of five chapters.

In chapter 1, the overview of the Lattice Gas Automata (LGA) and the Lattice Boltzmann Equation (LBE) methods are given. Different modifications of the LBE method are presented (the isothermal model, the model with variable temperature and the model with interparticle interactions). Some test computations were carried out.

A possibility to apply the LBE method to solve parabolic and elliptic equations is shown.

In chapter 2, the simulation of convective detonation waves in a porous medium is presented. Fuel forms initially a film on the pore walls. Pores are filled with oxidizer. Fuel evaporated from walls burns instantly. Computations was performed by the LGA method with additional simulation of exothermal chemical reaction, friction against the porous bed and heat losses. Computed wave velocity and pressure profile are in good agreement with experimental ones.

The chapter 3 deals with the simulation of mixing in a two-component system due to development of the shear flow instabilities. Flow evolution for different initial geometry was considered. The results obtained were used to compute the time dependence of the electric conductivity of detonation products of heterogeneous HE. The dependencies obtained were compared with experiment. The qualitative agreement of the experimental and computation data was shown.

Further, the modification of the LBE method to simulate electrohydrodynamic (EHD) flows is presented (chapter 4). Several methods to compute the convective charge transport were considered. Theoretical values of the numerical diffusivity were compared with computation results. Development of EHD-flow in different geometry was studied. In two-dimensional case, the flow has oscillatory character caused by the charge injection in discrete lumps that reduce the electric field. As the voltage between electrodes is increased, the liquid flow instability emerges which breaks the flow symmetry.

At certain conditions, the emergence of a region of gas phase was observed in computations. Such a bubble was generated in the region of high electric field (near the tip) due to to electrodynamic cavitation — homogenous nucleation in the region of low (or negative) pressure. The density inside the bubble decreased by three orders of magnitude. The time of bubble development increased with the decrease of electric field, this effect was of the threshold character. The electric breakdown of bubbles generated can result in the breakdown of liquid

by the bubble mechanism.

In chapter 5, the propagation of streamers and the dynamics of the electric discharge channel in liquid were investigated for planar and cylindrical cases. Divergent shock waves were observed at the channel expansion due to energy release in it and at the supersonic propagation of the streamer tip.

The inner structure of the channel boundary was considered, the transition layer "liquid–plasma". The non-monotonic pressure variation across the boundary due to viscous tension was shown. Theoretical estimates of the pressure jump on the channel boundary and of the pressure peak inside the transition layer agree well with computation results.

In the Conclusions chapter, the main results are formulated.

The results obtained are published in [1–14].

Chapter 1

Lattice methods in fluid dynamics

In the lattice methods, the fluid flow is regarded at the mesoscopic level as a dynamic of the system of special particles with simple properties.

The lattice gas automata (LGA) was for the first time proposed in 1976 [15]. There, the square lattice was used. This model has, however, some drawbacks, the main of them is the unphysical form of the pressure tensor caused by insufficient lattice symmetry. The rapid development of the LGA method began from the work [16] (1986), where the triangular lattice was introduced with the sufficient symmetry (at present, hundreds of papers were published).

The method of lattice Boltzmann Equation (LBE) has grown historically as a development of the lattice gases [17, 18]. This method progresses rapidly during last 15 years. It is very promising for simulation of subsonic liquid flows, especially flows in complex geometry and dynamics of multiphase fluids.

1.1 Lattice gas method

In the LGA method, fluid is modeled microscopically as a collection of particles moving on a regular lattice along the links. There is a small number of possible particle velocity vectors $\mathbf{c}_k$ $(k = 1, \ldots, b)$. The velocity of each particle points to one of the neighbor nodes, and it is chosen so as $\mathbf{c}_k \Delta t = \mathbf{e}_k$ where $\mathbf{e}_k$ are vectors linking the given node with its neighbors. That is, each particle moves exactly to one of the neighbor nodes at one time step. (In following, the distance between neighbor nodes and the time step Δt are assumed unity.) There are at most one particle with given velocity vector at the node (exclusion principle). Let us denote the number of particles moving in the direction of $\mathbf{e}_k$ by n_k. Its possible values are $n_k = \{0, 1\}$, therefore, the presence at a node of particle with given velocity vector can be coded by one bit, and the state of whole node

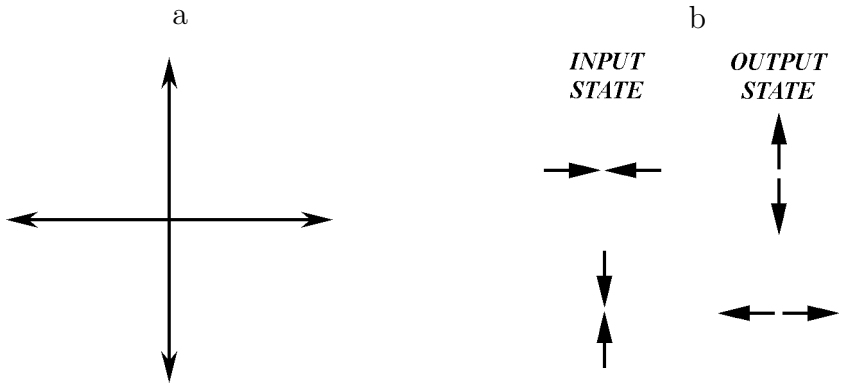

Figure 1.1. Possible velocity vectors in the HPP model (a) and possible collisions with different initial and final states (b)

— by b-digit binary number [1].

Time evolution of the system proceeds as follows. The complete time step consists of the propagation and collision sub-steps. At the propagation sub-step, each particle moves to the nearest node in the direction of its velocity. At the collision sub-step, all particles at a node interact and change their velocity directions thus that the number of particles (density $\rho = \sum_{k=1}^{b} n_k$) and the total momentum $\rho\mathbf{u} = \sum_{k=1}^{b} n_k\mathbf{c}_k$ are conserved. Each of the sub-steps can be realized using the pre-computed look-up tables. The evolution equation for the LGA method is given by

$$n_k(\mathbf{x} + \mathbf{e}_k, t + 1) - n_k(\mathbf{x}, t) = \Omega_k(n(\mathbf{x}, t)),$$

where $\Omega_k(n(\mathbf{x}, t))$ is the collision operator, i.e., the change in n_k as a result of collisions at a node. Thus, the lattice gas method is an extremely simplified version of the molecular dynamics method for the special particles with simple properties.

Historically, the first lattice gas model was the HPP model, named by its authors — Hardy, de Passiz, Pomeau [15]. Here, the square lattice is used, 4 possible velocity vectors exist (fig. 1.1,a). The only non-trivial collisions in the HPP model satisfying the conservation laws are easily seen to be "head-to-head" collisions resulting in the rotation of particle velocities by 90° (fig. 1.1,b). Unfortunately, the HPP model although behaves like a liquid, has some inadequate features. The cause of its shortcomings is the insufficient symmetry of

[1]The increase in the number of particles with given velocity vector is inexpedient because it leads to a significant complication of the computational scheme giving no substantial improvement. In the limit of $n_k = \{0, \ldots, \infty\}$, one obtains the same equations as in the lattice Boltzmann method which is substantially simpler and more obvious.

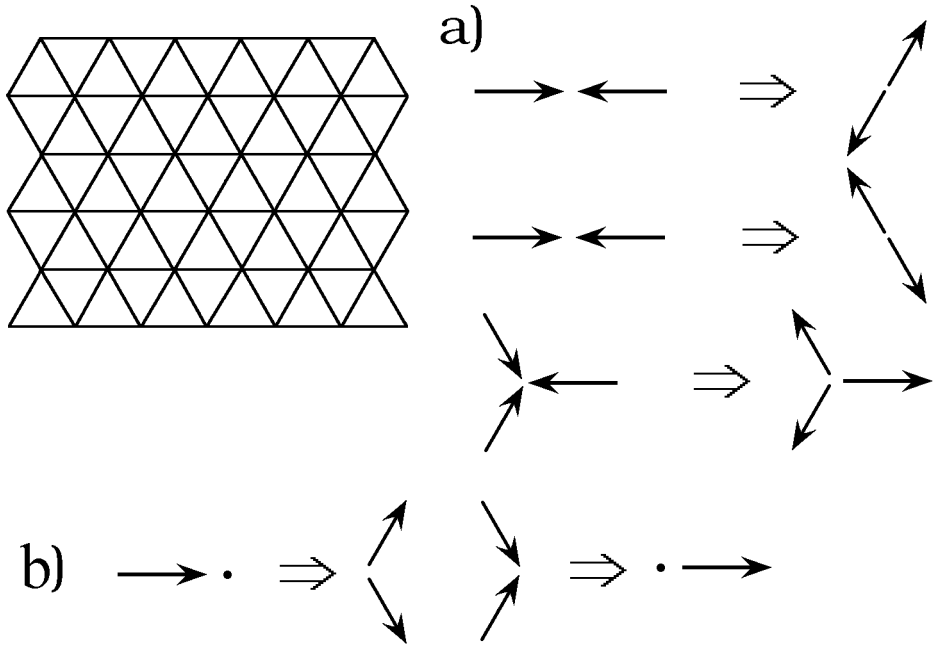

Figure 1.2. Lattice geometry and examples of possible collisions in the FHP-I model (a), some possible collisions with rest particles in the FHP-III model (b)

the square lattice. In particular, the momentum flux tensor is given by [19]

$$\Pi_{ik} = p\delta_{ik} + \rho g(\rho) \begin{pmatrix} u_x^2 - u_y^2 & 0 \\ 0 & u_y^2 - u_x^2 \end{pmatrix}.$$

Here $p(\rho)$ is the pressure, $g(\rho)$ is some coefficient. One can see, that the dynamic part of this tensor differs significantly from the usual form $\rho u_i u_k$.

Triangular lattice has, however, sufficient symmetry. The triangular lattice with $b = 6$ velocity vectors was used in [16] (FHP model — Frish, Hasslacher, Pomeau). In this case, the nontrivial collisions are the collisions of three particles with zero total momentum (the velocities are reversed after the collision), and the two- and four-particle collisions also with zero total momentum (in this case, the state is rotated by $\pi/3$ clockwise or counterclockwise, the direction is chosen randomly). This model is called FHP-I, the lattice geometry and some possible particle collisions are shown in fig. 1.2,a. The equation of state $p = \rho/2$ (up to the first order of u) corresponds to the ideal gas with constant temperature $T = 1/2$. Rest particles (at most one per site) can exist in the extended model FHP-III, also proposed in [16]. Rest particles can turn into moving ones in collisions, and vise versa (fig. 1.2,b). In this case, the pressure is $p = 3/7\rho$.

It was shown in [16], that this simple system simulates the equations of the

Navier–Stokes type (averaged over a macroscopic space-time region)

$$\frac{\partial u_\alpha}{\partial t} + g(\rho) u_\beta \frac{\partial u_\alpha}{\partial x_\beta} = -\frac{1}{\rho}\frac{\partial p}{\partial x_\alpha} + \nu(\rho)\Delta u_\alpha.$$

Here $g(\rho)$ is some coefficient (e.g., in the FHP-I model $g = (3-\rho)/(6-\rho)$), $\nu(\rho)$ is the kinematic viscosity, greek indices α, β denote cartesian coordinates, sum over repeated indices is assumed. The pressure is $p(\rho, u) = \rho/2 - \rho g u^2$.

In contrast with the HPP model, here the averaged equations are isotropic, the lattice structure is dropped out at the averaging. Similarly, high-symmetry crystals behave as isotropic solids.

Shortcomings of the model — the lack of Galilean invariance(coefficient $g(\rho) \neq 1$ before the convective term) and the unphysical velocity dependence of pressure origin from the form of the collision term. These drawbacks are insignificant for low-velocity flows. In almost incompressible case, one can get rid of the coefficient $g(\rho)$ by the velocity rescaling [16].

The use of the square lattice is possible that is more convenient as the triangular one but this requires to increase the number of states. The square lattice was used in [20] with the possible velocity values of 0 (the number at a node n_0, the energy 0), 1 (n_1, the energy 1/2), and $\sqrt{2}$ (n_2, the energy 1). There are 9 possible velocity vectors, and particles have unit mass. In this model, it is possible to introduce besides the density $\rho = n_0 + n_1 + n_2$ and momentum, the full energy at a node $E = n_1/2 + n_2$, the pressure $p = E - \rho u^2/2$, and the temperature $T = p/\rho$. In this case, the energy conservation should also hold in collisions. Some examples of collisions are shown in fig. 1.3.

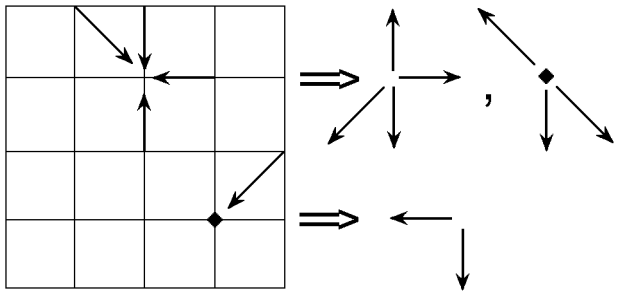

Figure 1.3. Lattice geometry and collision examples for the square lattice

A great advantage of the lattice gas method is the use of integer arithmetics only. Besides the computation acceleration and economy of memory, it leads to absence of round-off errors and absolute numerical stability. It is easy in the lattice gas method to set boundary conditions of any type. For instance, at fixed boundaries one can rotate velocity of arrived particles by 180°. In this way, no-slip boundary conditions are simulated.

The main drawback of the LGA method is the substantial statistic noise. It makes necessary to average computation results over large spatial regions, or for long time intervals, or over many copies of the system (ensemble averaging).

Moreover, there is no regular lattice with necessary symmetry in a three-

dimensional space. Therefore, it was suggested to simulate three-dimensional flows with use of the four-dimensional lattice (face-centered hypercubic) with one layer and periodic boundary conditions in the fourth dimension [21]. Then, the velocities are projected to the three-dimensional space. In this model (denoted 4D FCHC), there are 24 velocity vectors that greatly complicates the collision table (even when each collision has the single result, the size of the table is $3 \cdot 2^{24} = 48$ MB). Another variant also introduced in [21] uses the three-dimensional cubic lattice and three values of velocity 0, 1, and $\sqrt{2}$, 19 velocity vectors at the whole. In this case, the total energy should also be conserved at collisions.

To simulate multiphase and multicomponent flows, the models with inter-particle interactions were developed. The interaction can be both a repulsion between particles of different types at one node that leads to the separation of immiscible liquids [22], and a long-range attraction between particles at different nodes that allows one to simulate phase transitions [23]. The review of this class of models is given in [24].

1.2 Lattice Boltzmann equation method

The lattice Boltzmann equation method was at first developed from the LGA method [17, 18]. Later, it was directly derived from the continuum Boltzmann equation [25–29], that strengthened the theoretical basis of the LBE method significantly.

The basic idea of the LBE method is the ensemble averaging in order to get rid in principle of the statistic noise. This enables to reduce significantly the number of nodes in the computation region. The one-particle distribution functions N_k (real variables) which are the ensemble-averaged values of occupancies are used instead of binary occupancy values. Their evolution proceeds formally in the same way as in the LGA model, i.e., equations are given by

$$N_k(\mathbf{x} + \mathbf{e}_k, t + \Delta t) - N_k(\mathbf{x}, t) = \Omega_k(N(\mathbf{x}, t)), \tag{1.1}$$

where Ω_k is the collision operator. In fact, the Boltzmann kinetic equation for a certain simple model system is solved. Like LGA, the LBE method results in the Navier–Stokes equations after averaging over a space-time region.

In early works, the same collision operator as in the LGA method was used [17] (the collision operator corresponds to the collision integral in the linetic equation). Such scheme inherits all shortcomings of the LGA method — the lack of Galilean invariance and the unphysical velocity dependence of pressure.

Moreover, the collision operator consists in this case of a sum of polynoms in the form of $\prod_{k=1}^{b} N_k^{\alpha_k}(1-N_k)^{1-\alpha_k}$, $\alpha_k = \{0,1\}$, this leads both to the large number of arithmetic operations, and to the significant roundoff errors. The linearized form of the collision operator was introduced in [18] obtained by the expansion of distribution functions around their equilibrium values N_k^{eq} for the case of small Mach and Knudsen numbers. The linearized collision operator is given by $\Omega_k = \sum_{j=1}^{b} M_{kj}(N_k - N_j^{eq})$, where $\|M_{kj}\|$ is a matrix $b \times b$. It was shown in this work that taking into account the lattice symmetry and the mass and momentum conservation laws, the matrix $\|M_{kj}\|$ contains only two independent elements for the FHP-I model, and three — for the FHP-III and 4D FCHC models.

Presently, the BGK-form of the collision operator is mainly used, that was introduced for the problems of physical kinetics in 1954 (Bhatnagar, Gross, Krook [30]). It is the relaxation to the local equilibrium

$$\Omega_k(N) = -(N_k - N_k^{eq})/\tau, \tag{1.2}$$

i.e., the collision matrix is reduced to the simplest form $M_{kj} = -\frac{1}{\tau}\delta_{kj}$. The relaxation time τ governs the transport coefficients: viscosity (kinematic viscosity ν), heat conductivity and diffusivity D. Values of $\tau < 1$ imply upper relaxation. This form of the collision operator ensures Galilean invariance and can be easily extended to the three-dimensional case [31].

Equilibrium distribution functions N_k^{eq} depend on the density $\rho = \sum_{k=1}^{b} N_k$ and the mass velocity at a site $\mathbf{u} = \sum_{k=1}^{b} N_k \mathbf{c}_k/\rho$ thus that the mass, momentum and energy conservation laws are satisfied at collisions. Equilibrium distribution functions are usually chosen in the Maxwellian form: $N_k^{eq} \sim \exp(-(\mathbf{c}_k-\mathbf{u})^2/2T)$ (particle mass is assumed unity, $m = 1$). Expanding the exponential up to $O(u^2)$ one obtains

$$N_k^{eq} = \rho w_k \left(1 + \frac{\mathbf{c}_k\mathbf{u}}{T} + \frac{(\mathbf{c}_k\mathbf{u})^2}{2T^2} - \frac{u^2}{2T}\right).$$

Weight coefficients $w_k \sim \exp(-\mathbf{c}_k^2/2T)$ depend only on the value of $|\mathbf{c}_k|$.

Following equations should hold:

$$\sum_{k=1}^{b} N_k^{eq} = \rho, \qquad \sum_{k=1}^{b} N_k^{eq}\mathbf{c}_k = \rho\mathbf{u}, \qquad \sum_{k=1}^{b} N_k^{eq}\mathbf{c}_k^2 = \rho(Td + u^2).$$

Here d is the dimension of space. After the substitution of the expansion of N_k^{eq}, one should separately equate the coefficients at each power of u.

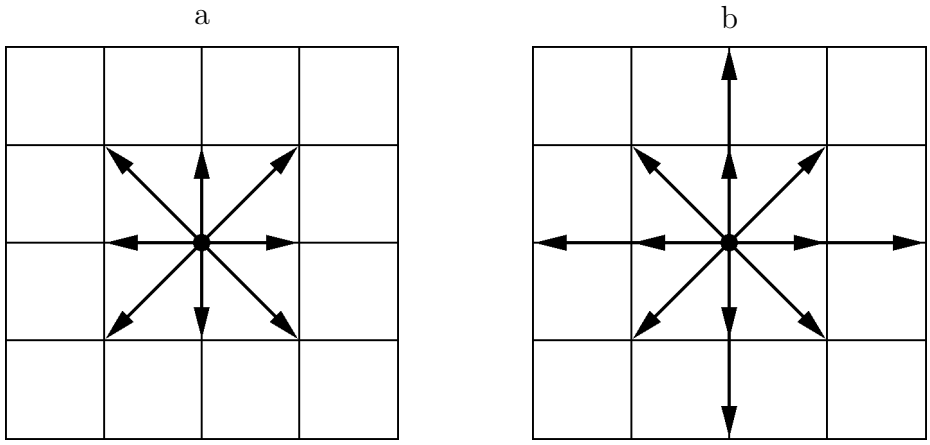

Figure 1.4. Lattice geometry and possible velocity vectors. *a* — the model with 3 velocity values (9 velocity vectors, isothermal model), *b* — the model with 3 velocity values (13 velocity vectors, variable temperature) [32]

For the one-dimensional model, $\mathbf{c}_0 = 0$, $\mathbf{c}_1 = -1$, $\mathbf{c}_2 = 1$, and one obtains $T = 1/3$, $w_0 = 2/3$, $w_{1,2} = 1/6$. In the two-dimensional model at the square lattice with 9 directions (fig. 1.4,*a*), three values of particle velocity 0, 1 and $\sqrt{2}$ are possible. This adds one more equation $w(0)/w(1) = w(1)/w(\sqrt{2})$. The solution gives $T = 1/3$, $w(0) = 4/9$, $w(1) = 1/9$, $w(\sqrt{2}) = 1/36$. Such models describe isothermal liquid flows. The sound velocity is $c_s = \sqrt{T} = 1/\sqrt{3}$. At low velocity, the liquid can be considered almost incompressible (compressibility effects are proportional to the second order of Mach number).

Using the Chapman–Enskog expansion [33] up to $O(u^2)$ of equations (1.1) and (1.2), the Navier–Stokes equations for incompressible liquid are obtained:

$$\frac{\partial \rho}{\partial t} + \frac{\partial \rho u_\alpha}{\partial x_\alpha} = 0,$$
$$\frac{\partial \rho u_\alpha}{\partial t} + \frac{\partial \rho u_\alpha u_\beta}{\partial x_\beta} = -\frac{\partial p}{\partial x_\alpha} + \nu \frac{\partial}{\partial x_\beta}\left(\frac{\partial \rho u_\alpha}{\partial x_\beta} + \frac{\partial \rho u_\beta}{\partial x_\alpha}\right),$$

here $p = \rho c_s^2 = \rho/3$ is the pressure, $\nu = (\tau - 1/2)/3$ is the kinematic viscosity [31]. In the absence of interparticle interaction, one obtains also $D = \nu = (\tau - 1/2)/3$. The stability condition is $1/2 < \tau < \infty$, that is equivalent to $D > 0$, $\nu > 0$. The equations obtained are exact, up to $O(u^2)$ [34].

The lattice Boltzmann equation was theoretically investigated in [35] in the case of finite Mach numbers, when the compressibility can not be neglected. The expression for the bulk viscosity was obtained, the formulas for the equilibrium distribution functions were introduced which allows one to adjust arbitrarily the bulk viscosity.

The LBE method was shown in [36] to be of second order of accuracy both over the space and time. The Courant number is $\lambda = \Delta t|\mathbf{c_k}|/|\mathbf{e_k}| = \mathbf{1}$, i.e.,

the method is marginally stable that leads to numerical instabilities at low viscosities. A simple way to overcome this instability was suggested in [37, 38]. It consists of the use of the reduced effective time step with further interpolation of distribution functions to the lattice sites. Along with the improved stability, this scheme leads to reducing the effective viscosity that allows one to increase the efficiency of simulations of flows with high Reynolds numbers.

The BGK-LBE method is widely used to simulate viscous flows [39, 40], see also the review [36]. The flow around the cylinder was simulated in [40] with Reynolds numbers up to 10^4. In this work, the additional interpolation step was introduced allowing one to use spatially nonuniform grid corresponding to the cylindrical geometry. In the works above, the results of computations by the LBE method were compared with the results obtained by other methods (in [39]), and also with the experiments (in [40]). The results agree well in all cases. An extensive comparison of the LBE method with spectral and finite-difference ones can be found in [41].

Another example of the use of the non-uniform spatial grid and the additional interpolation step can be found in [42]. The non-uniform grid and the combination of the LBE method with the finite-volume method was used in [43, 44] (finite-volume LBE, FVLBE). The method of local grid refinement with the use of a decreased time step in regions with the fine grid was suggested in [45]. In the next work of the same authors [46], it was shown that such grid refinement can lead to a significant acceleration of computations. The use of the multigrid model can also improve the efficiency of computations [47].

Different modification of the Lattice Boltzmann equation method exist which allows one to simulate, for example, problems of the magnetic hydrodynamics [48, 49], dynamics of a viscoelastic medium [50] and flows in a porous medium [51]. The most important of them are, however, the models describing the flows with variable temperature and the dynamics of multiphase and multicomponent fluids.

1.3 Simulation of thermohydrodynamic flows

Using the larger number of the velocity values in the LBE method makes it possible to introduce the local fluid temperature. In this case, equilibrium distribution functions depend on the temperature and the simulation of thermohydrodynamic flows becomes possible [52] — in this work the triangular lattice with three possible velocity values 0, 1, and 2 was used. The square lattice was used in [32, 53]. An example of lattice geometry and possible velocity vectors

for the two-dimensional case is shown in fig. 1.4,*b*. Other possible sets of particle velocities were introduced in [54]. The thermal diffusivity χ is uniquely coupled in such models with the relaxation time τ, i.e., the Prandtl number $\mathrm{Pr} = \nu/\chi$ is fixed. A generalized collision operator was introduced in [55] that allows one to simulate fluids with arbitrary Prandtl number.

This method is, however, stable only in the narrow range of temperature and velocity [56]. One of possible optimization ways is the modification of velocity set and its "decoupling" from the spatial lattice [56, 57].

Another way is the change of the equilibrium distribution functions. Instead of the expansion of Maxwellian distributions up to fourth order in velocity necessary to describe properly viscous terms in thermal flows [53], it was suggested to specify a dependence between distribution functions for different velocity values. In the special case of one-dimensional model with velocities $c_0 = 0, c_{1\pm} = \pm 1, c_{2\pm} = \pm 2$ this dependence was specified as $N_{2\pm} = \lambda_\pm N_{1\pm}$, where coefficients $\lambda_\pm = -\frac{(c_{2\pm}-u)^2-(c_{1\pm}-u)^2}{2T}$ correspond to the Maxwellian distribution [58]. This scheme allows one to extend the stability region of the method.

The variant of the LBE method proposed in [38] also allows one to increase the stability of thermohydrodynamic computations.

At present, other methods were developed for simulation of the thermal flows. One of them is based on the passive scalar transport of the temperature [59]. The more detailed description is given in section 1.5. This method is applicable to simulate inviscid flows. Its main shortcoming is that viscous heat dissipation and compression work are not taken into account. Another way is to introduce additional distribution functions for the internal energy [60, 61]. Evolution of these functions proceeds according to the LBE-like equation, viscous heat dissipation and compression work done by the pressure can be incorporated [60]. Density and momentum at a node are calculated using the LBE distribution functions for the substance. The internal energy dependence of the equilibrium state can be introduced allowing one to simulate substances with desired equation of state (e.g., the ideal gas or the Van der Waals one) [61].

1.3.1 Connection between the LBE method and differential equations

The LBE model corresponds to the system of partial differential equations for distribution functions (see, e.g., [57])

$$\frac{\partial N_k}{\partial t} + \mathbf{e}_k \cdot \nabla N_k = \Omega_k \qquad (k = 1, 2, \ldots, b).$$

This system is linear, and it can be solved by any hyperbolic solver [57, 62]. This method allows one, for example, to stabilize the unstable thermal models by introducing the artificial diffusion and viscosity [62].

Rather different approach was developed in [63]. Here, the overrelaxation was introduced at the propagation step. It was shown, that this results in the improved stability of the thermal model against long-wave perturbations due to additional numeric viscosity and heat conductivity. In some range of temperature, the model is also stable against short-wave perturbations.

1.4 Simulation of multiphase and multicomponent flows

The LBE method for simulation of immiscible liquids was firstly developed similarly to the LGA method [64, 65]. Additional forces near the interface were supplemented to the standard model along with the re-distribution of particles of different types on lattice directions, also near the interface in order to obtain the flux of particles of one type to the nodes with the majority of the same type of particles. In such models, the effective mutual diffusivity is negative. A model of partly miscible liquids with adjustable diffusivity was introduced in [66] based on this approach.

In another variant of the LBE method, an interaction was introduced between particles at different nodes (attraction or repulsion) [67–70]. Let us consider a system consisting of S different components (the case of one-component system, $S = 1$ is also included). We denote the component number by the index "s". In the simplest case, interaction exists between the nearest neighbors only. Interaction force is given by:

$$\Delta(\rho_s \mathbf{u}_s)/\tau_s = \mathbf{F}_s(\mathbf{x}) = -\sum_{s'=1}^{S} G_{ss'}\psi(\rho_s(\mathbf{x}))\sum_k \mathbf{e}_k \psi(\rho_{s'}(\mathbf{x}+\mathbf{e}_k)).$$

Here $\rho_s = \sum_k N_{sk}$, $\rho_s \mathbf{u}_s = \sum_k N_{sk}\mathbf{e}_k$ are density and momentum of component number s at the node $\mathbf{x}$. Interaction strength between different components is specified by the matrix $\|G_{ss'}\|$. If the element $G_{ss'} < 0$, there is an attraction between components s and s', otherwise — a repulsion. "Effective mass" $\psi(\rho)$ should be an increasing function of ρ. In computations, we assumed $\psi(\rho) = \rho_0(1 - \exp(-\rho/\rho_0))$ (ρ_0 is some constant) [67].

Action of the force leads to the change of velocity at a node:

$$\Delta \mathbf{u}_s = \mathbf{F}_s \tau_s / \rho_s.$$

The equilibrium distribution functions for the collision operator are calculated using the changed velocity $\mathbf{u}_s = \mathbf{u}' + \Delta \mathbf{u}_s$. For the mass and momentum

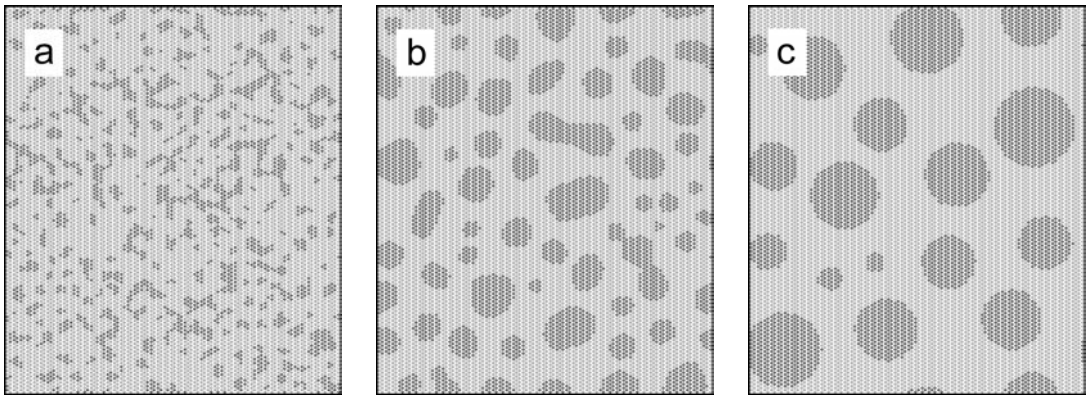

Figure 1.5. Spinodal decomposition of two immiscible liquids. $t = 6$ (a), $t = 200$ (b), and $t = 14200$ (c). Lattice size is 80×80 sites, horizontal and vertical boundary conditions are periodic

conservation laws to hold at collisions, the "common velocity" $\mathbf{u}'$ should be expressed as [69]

$$\mathbf{u}' = \frac{\sum\limits_s \rho_s \mathbf{u}_s/\tau_s}{\sum\limits_s \rho_s/\tau_s}.$$

The diffusion coefficient for multicomponent model were obtained in [69,70] in dependence on the interaction matrix $\|G_{ss'}\|$.

In this work, because of use of the square lattice (in contrast with the triangular one used in [67–70]), the interaction was also introduced between particles separated by $\sqrt{2}$, at that

$$G_{\Delta x=\sqrt{2}} = \frac{1}{8} G_{\Delta x=1}. \tag{1.3}$$

This corresponds to the force decreasing with distance as $F \sim r^{-6}$.

As a test, the spinodal decomposition was simulated — segregation of a mixture of two immiscible liquids (fig. 1.5). Here, the repulsion between different components was introduced ($G_{11} = G_{22} = 0$, $G_{12} = G_{21} > 0$).

In a certain density range, the denser substance ("liquid") can be in the equilibrium with its "saturated vapor". For this to be possible, a sufficiently strong attraction between particles should exist. Let us consider the one-component fluid and denote $G_{11} = G$. The pressure is given by formula [67]

$$p = \rho RT + \frac{b}{2} G \psi^2(\rho).$$

The critical point is determined from the equations [67]:

$$\frac{\partial p}{\partial \rho} = RT + bG_c \psi \psi' = 0,$$

$$\frac{\partial^2 p}{\partial \rho^2} = bG_c(\psi \psi' + \psi'^2) = 0,$$

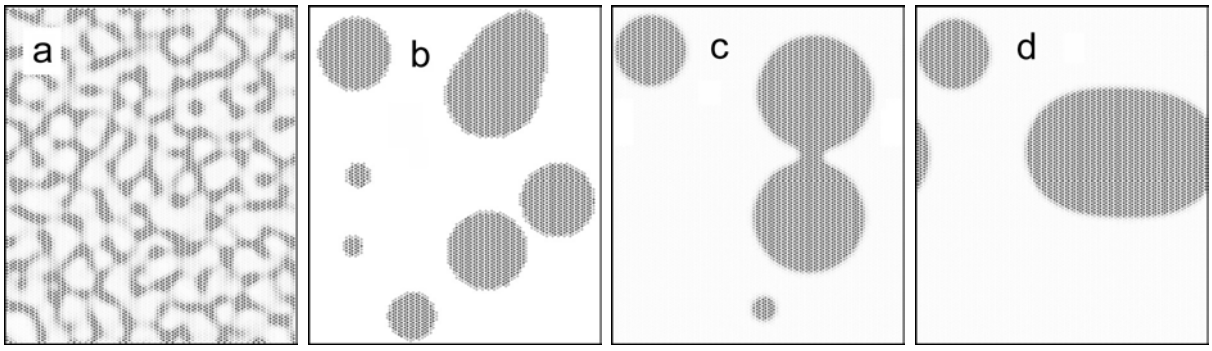

Figure 1.6. Transition from the metastable uniform state to the two-phase system "gas–liquid". $t = 26$ (a), $t = 1340$ (b), $t = 5190$ (c), and $t = 5900$ (d). Lattice size is 80×80 sites, boundary conditions at X and Y are periodic

which are analogous to the equations for the inflection point at the critical isotherm. Obviously, the simplest dependence $\psi(\rho) = \rho$ does not allow one to describe a phase transition. For the effective mass $\psi(\rho) = \rho_0(1 - \exp(-\rho/\rho_0))$, simple calculations give the critical values of $\rho_c = \rho_0 \ln 2$, $G_c = -4RT/b\rho_0$ [67]. The increase in absolute value of G is analogous to the decrease in temperature in the case of real matter.

In our case, because of use of the square lattice and two different interaction coefficients (equation (1.3)), the pressure is given by:

$$p = \frac{\rho}{3} + \frac{5}{4} G\psi^2(\rho).$$

From this equation, the critical values are $\rho_c = \rho_0 \ln 2$, $G_c = -8/15\rho_0$. Test computations were carried out which gave the value $G_c \approx -0.535$ for $\rho_0 = 1.0$ that correspond with the theoretical prediction within 0,5%.

Figure 1.6 shows the transition from the metastable uniform state to the system "liquid–gas". The formation and growth of drops is observed due to both the coalescence (fig. 1.6,c), and the evaporation of smaller drops and the vapor condensation on larger ones (fig. 1.6,b–d). At the coalescence of large drops, the form oscillations due to the surface tension are readily observed (fig. 1.6,c,d).

By a slight modification of the collision operator, a simulation of liquid-phase chemical reactions becomes possible [71]. At that, some interesting phenomena arising in reaction-diffusion systems are observable: oscillatory regimes, self-organization (generation of stable spatially non-uniform structures), autowaves, etc.

The lattice Boltzmann equation for nonideal gases was theoretically derived in [27–29] from the Enskog equation (modified Boltzmann equation for dense gases). It was shown that the expression obtained coincide with the equations of

the model introduced in [67–69] up to the terms of second order in the velocity and the interaction force. The modification of the method introduced in [27] was used in [72] to simulate three-dimensional Rayleigh–Taylor instability of two immiscible liquids.

1.5 Transport of passive scalar

A natural way exists to incorporate to the LBE method a transport of a passive scalar (admixture that does not affect the main flow). For that, an additional component with zero mass is introduced presented in the same from as the main substance. The evolution equations for the distribution function of a scalar f_k are similar to the equations for N_k:

$$f_k(\mathbf{x}+\mathbf{e}_k, t+1) - f_k(\mathbf{x}, t) = -\frac{1}{\tau_n}(f_k(\mathbf{x}, t) - f_k^{eq}(\mathbf{x}, t)).$$

The equilibrium values f_k^{eq} depend on the scalar concentration at a node $n = \sum\limits_k f_k$, and on the velocity $\mathbf{u}$ of the substance at a node (as before, $\mathbf{u} = \left(\sum\limits_k N_k \mathbf{e}_k\right) / \left(\sum\limits_k N_k\right)$, i.e., the component corresponding to the scalar introduces the zero contribution to the momentum). Thus, the transport equation for a passive scalar is obtained

$$\partial n/\partial t + \operatorname{div}(n\mathbf{u}) = \operatorname{div}(D_n \nabla n).$$

The diffusivity of passive scalar is $D_n = (\tau_n - 1/2)/3$, it can be chosen independent on the fluid viscosity. In low-velocity flows, fluid can be considered incompressible, div $\mathbf{u} = 0$, and the transport equation is given by

$$\partial n/\partial t = \mathbf{u} \cdot \nabla n + \operatorname{div}(D_n \nabla n).$$

A certain disadvantage of this method is an increased amount of memory necessary for computations. This method was used, e.g., to calculate temperature in simulation of Rayleigh–Benard convection in [59].

1.6 Use of the LBE method to solve parabolic and elliptic PDEs

The variant of the LBE method described in previous section can be of independent applicability. If the flow velocity is set to zero in the whole region, the equation of parabolic type is obtained:

$$\partial n/\partial t = \operatorname{div}(\chi \nabla n).$$

Therefore, the use of this method to solve, e.g., the heat conduction equation is possible, one should only specify proper boundary conditions (in this case, n corresponds to the temperature). The thermal diffusivity $\chi = (\tau_n - 1/2)/3$ can vary over the space and time. The stability condition is $\chi > 0$. It it interesting to compare this result with the stability condition for explicit scheme $0 < \chi \Delta t/\Delta x^2 < 1/2^d$, where χ is bounded also from the other side. However, at large values of χ, the LBE method is though stable, but it gives a solution significantly different from the exact one.

If the boundary conditions are time-independent, the stationary distribution is obtained asymptotically which satisfies the Laplace equation $\mathrm{div}(\chi \nabla n) = 0$. This technique is similar to the relaxation method, it can be used to solve elliptic equations.

Thus, the LBE method is flexible and sufficiently universal computation tool to simulate different processes in fluids.

In following chapters, the LGA and LBE methods are applied to solve different hydrodynamic and electrohydrodynamic problems.

Chapter 2

Simulation of convective detonation waves in a porous medium

Peculiar detonation-like flows in rigid porous media were observed in [73–78]. The active component of such media can be a gas mixture that fills pores [73] or a layer of a high explosive (HE) on the pore surface [78] or a fuel film [74–77].

The wave regimes of combustion in a rigid porous medium are characterized by a complex wave front, which is a random pulsating relief of hills and valleys, and by a smooth increase in pressure. The average front velocity is ≈ 1 km/s. The front pattern and the pressure profile are shown schematically in fig. 2.1.

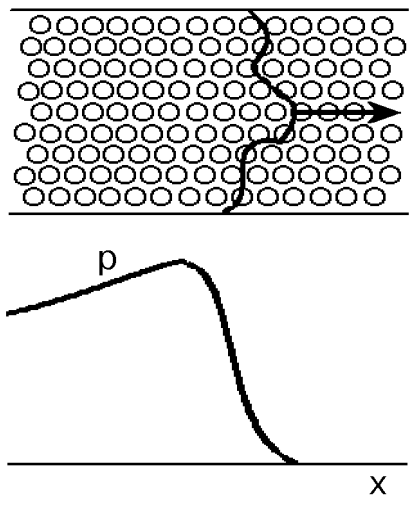

Figure 2.1.

In opinion of authors of experimental works, the waves propagate by a convective or jet mechanism. The wave-propagation conditions are strongly affected by the porous bed. Because of friction losses, the wave velocity is not sufficient to initiate a reaction by the standard shock-wave mechanism. Instead, ignition is ensured by hot gas jets that burst ahead of "average" front from the combustion zone.

Previously, similar conclusions were made for a different system — a porous explosive [79, 80]. Some initiation regimes, such as an electric discharge or explosion of a conductor inside HE, injection of hot combustion products from a separate chamber upon rupture of a membrane or the action of gas-detonation products on a powder, also generate a wave with a velocity of ≈ 1 km/s and a pressure of ≈ 2 kbar. In charges of small diameter (3–4 mm) with a very light shell, this wave is rather stable; here a smooth increase in pressure and forma-

tion of jets were also observed. Although the low strength of HE leads to slight deformation of the porous bed, available data also suggest a jet mechanism of wave propagation. From the pressure level, the burnt fraction of the material is estimated at several percent, i.e., the concentration of the reacted HE is close to that used in the experiments of [78].

In this work, we consider a system in which a gaseous oxidizer in pores reacts with a fuel film on the surface of the pore structure [74–77]. Physically, an active porous medium of the "gas–film" type can be, for example, sand or packing of rigid granules, with pore walls covered by a thin film of fuel that can react with pore-filling oxidizer. The initiation of such a system is possible by the "shock" of a gas detonation.

2.1 Discrete model of convective wave

The flow of gas was simulated by the LGA method (see chapter 1). For flow in a porous medium, the drawbacks of this model are insignificant because the flow velocity is low due to friction. Of course, simulation of fast jets can be only qualitative, but today this is true for deterministic finite-difference methods. Some results of application of the isothermal FHP lattice model to the problem of convective waves are reported in [81, 82]. These papers deal with the case of "isothermal detonation", where the active component is an explosive. In this case, the temperature of the gas (reaction products) in the combustion zone is constant.

For gas-film detonation in the reaction zone, the temperature is obviously variable. It increases during fuel burnup from the low initial temperature of the oxidizer to the temperature of combustion products. It is clear that the isothermal FHP model is inapplicable to this system.

Therefore, we implemented a nine-velocity version of the method on a square lattice [20], which is schematically shown in fig. 1.3. Particles move along the sides of the square (density n_1, velocity 1, and energy 1/2) or its diagonals (density n_2, velocity $\sqrt{2}$, energy 1). Each of these eight states can be occupied by one or none particle. In addition, there are rest particles (density n_0), whose number may in principle be arbitrary (in our computations, it is not more than six). The system simulates a two-dimensional gas with density $\rho = n_0 + n_1 + n_2$ and pressure $p = n_1/2 + n_2 - \rho u^2/2$. The presence of three "energy levels" makes it possible to introduce a variable temperature $T = p/\rho$. The "diagonal" particles correct to some extent the disadvantages of the square lattice by producing nondiagonal components of the momentum flux.

A standard lattice step in time includes propagation of particles to neighbor nodes and collisions at nodes. The result of collision is chosen randomly out of all possible states that have the same number of particles, momentum, and energy and are not identical to the initial state (when present). A table of possible states is calculated before computation. Some examples of collisions are shown in fig. 1.3.

A gas-dynamic block (propagation + collision) was tested in special computation. Averaged values of the momentum flux tensor Π_{ik} were calculated for specified equilibrium states. They were close to $p\delta_{ik}$ — the main term. The inertial terms were of the order of $\rho u_i u_k$, although the coefficients depended significantly on the distribution of particles over the levels (i.e., on the temperature). For flow in a porous medium, the error in describing these components, which are quadratic in velocity, is insignificant because the velocity is low due to friction (~ 0.1).

In addition, a velocity of propagation of small perturbation over a homogenous state was determined. In the range studied, the propagation velocity of a "step" perturbation was nearly constant (between 0.9 and 1, although the temperature in test computations varied by at least an order of magnitude. This is a consequence of the inaccuracy of the model, namely the limited number of possible states.

A decrease in temperature (achieved by the prevalence of rest particles) did not lead to a noticeable decrease in wave velocity because perturbations were transferred by moving particles, whose velocity along the lattice axes is equal to unity. An "ideal" dependence $c = \sqrt{2P/\rho} \sim \sqrt{T}$ might be expected for very long waves when the flow has a chance to attain local thermal equilibrium. For the problem considered, such waves are of no interest.

A complete cycle of computation ignoring heat losses consists of four steps. Along with propagation and collisions, it includes a reaction and friction against the porous bed. Combustion was simulated by introducing two sorts of gas particles: "blue" particles (oxidizer) and "red" particles (combustion products). Initially, the pores contain only the oxidizer. Fuel (which forms a film on the pore walls in the physical system) participate in the computation as a source of particles that "evaporate" into the gas. In the simplest case, the reaction at each node involves formation of two high-energy "red" product particles from one rest "blue" particle and one fuel particle. "Red" particles cannot turn into "blue" particles (the reaction is irreversible) but "red" and "blue" particles can exchange energy during collisions. This simulates the process

$$A + B \longrightarrow 2C$$

with the energy effect equal to 2. At a given node, combustion begins when a certain condition is satisfied (for example, upon reaching specified temperature and pressure averaged over the nearest neighborhood of the given node) with given probability of the reaction w. For each node, once combustion began, the ignition condition was not further verified. This corresponds to the irreversibility of ignition in a given pore.

Reaction at the "burning" node occurs with the same probability w. The introduction of this parameter reflects to some extent the nonuniformity of the sizes and geometry of real pores, which should affect ignition and combustion. In most computations, we used the value of $w = 0.5$. Naturally, for the reaction, it is necessary that unexpended fuel, oxidizer, and two free diagonal states be present at a given node.

If three or four free diagonals were available, three diagonal product particles were formed (reaction $A + 2B \longrightarrow 3C$) from one fuel particle and two rest oxidizer particles (naturally, if they were present). This improves the stoichiometry because conventional fuel (for example, of gross-composition CH_2) is markedly lighter than the oxidizer ($1.5O_2$). For four free diagonals, new particles were randomly directed.

The last step of the cycle simulated friction. In the range of interest to us, the friction force is proportional to the squared velocity:

$$\mathbf{f} = -k\frac{\rho u \mathbf{u}}{d},$$

where d is the particle size of the porous bed and k is the friction coefficient. According to [83], $k = 1.75(1-\varphi)/\varphi^2$, where φ is the porosity (about 0.4 for loose packing). According to more recent data [84], the friction coefficient is approximately half the indicated value. Therefore, we assumed $k = 3.5$.

To use the friction law in the discrete system, we consider the deceleration of gas in one time step. For spatially uniform case, one can write $\rho \partial u/\partial t = f$, which leads to

$$\frac{du}{u^2} = -k\,dt\,.$$

Integrated over time interval τ, this equation results in

$$\Delta u = u(\tau) - u = -\frac{\tau k u}{d + \tau k u}.$$

This deceleration would be achieved on average, if we introduce the probability of velocity change

$$w = \frac{|\Delta u|}{u} = \frac{\tau k u}{d + \tau k u}.$$

The velocity at each node should be put to zero with the probability w. For each node, we calculated the local flow velocity u (averaged over nine points — a node and eight nearest neighbors). Then, the state at the node was replaced with probability $w = \tau ku/(d + \tau ku)$ by a new one with the same number of particles and the same energy but a random value of the momentum, so that, on the average, the velocity in the new state became zero. This procedure simulates loss of momentum in quadratic friction in time step τ. At the same time, the stochasticity of flow in a porous medium is simulated. The time step τ was always considered unit. In most of the computations, $d = 1$.

2.2 Computation results

Although the computations were performed in dimensionless form, it is conveniently to assume that the lattice spacing is 1 mm and the time step is 1 mks. The velocity is then expressed in km/s. For the density, any scale can be adopted, and the pressure is then expressed in the units of ρu^2. For example, if the unit of density corresponds to 10^{-3} g/cm^3 = 1 kg/m^3, the unit of pressure is 1 MPa. For temperature, the reasonable coefficient of conversion can correspond to 3000 K per unit.

We used a lattice with $1 \le x \le 250$ and $1 \le y \le 125$. On the top and bottom boundaries, periodic boundary conditions were imposed, and the right and left boundaries were rigid walls. Initial concentrations of the fuel f and oxidizer ("blue" particles) were specified: in the standard version, $f = 1.5$, $n_0 = 3$, $n_1 = 0.8$, $n_2 = 0.32$. Moving particles were distributed according to the probability of occupation. For the rest particles and the fuel (n_0 and f), the integer part was first distributed uniformly, and the fractional part, when present, was then randomly distributed. After several collisions, equilibrium was established in the gas. The initial concentrations are close to the equilibrium values corresponding to the specified density and energy.

Then, combustion was initiated by specifying a hot region with larger values of $n_1 = 1{,}2$ and $n_2 = 0{,}96$ for $x < 7$ (which corresponds to an increase in pressure by a factor of 2.17 and an increase in temperature by a factor of 1.73). At an ignition temperature of 0.4, a threshold pressure of 2.1, and a probability of reaction of 0.5, this perturbation developed into a quasistationary wave that "forgot" the initial conditions. An example of computation is shown in fig. 2.2.

The wave is obviously nonuniform, especially at the beginning. This is a consequence of the randomness in the initial conditions. At $t = 50$, the hot region looks like two "peninsulas". In fact, because of vertical periodicity, this

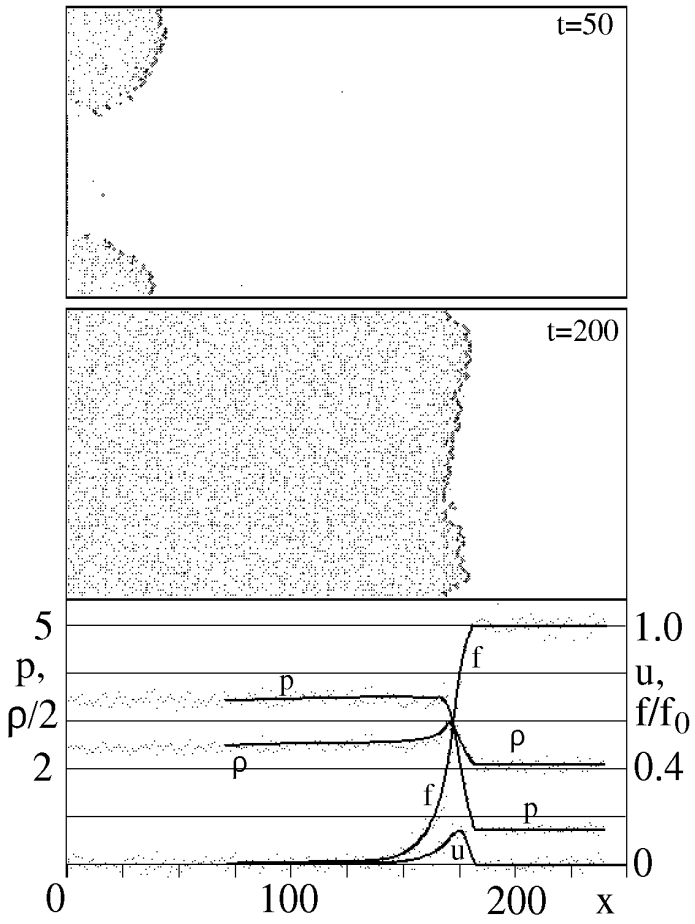

Figure 2.2. Position of the wave front (ignition sites) and qualitative distribution of local pressure for various times after the beginning of propagation: nodes at which $p > 4$ are shown, and for the last time, the averaged wave structure is presented

is one hot zone. The front is later smoothed but even after attainment of a quasistationary regime, it does not become completely flat. At the bottom of the figure there are plots of pressure, fuel concentration, density and velocity averaged over the vertical coordinate[1] (for example, $\langle p(x)\rangle = \sum_{y=1}^{125} p(x,y)/125$). For the given kinetics, the increase in the average pressure is smooth and corresponds to the region over which the wave front "is smoothed".

The average wave velocity was measured from the shift of the pressure profile from the time $t = 100$ and at $t = 200$, it was 0.93 km/s (in natural units), which is larger than the perturbation velocity in the initial state (0.9) but smaller than that in products (1.0). This corresponds to experiments with the only difference being that in the lattice gas, the range of sound velocities is very narrow. The flow velocity, as noted above, is about 0.1.

The increase in density corresponds to injection of fuel. At the wave front there is a small peak due to local compression.

As the probability of reaction w increases to 1, a flatter wave front is obtained; accordingly, the pressure rise is sharper. The wave velocity is $D = 1.19$.

[1]Letters p, u, ρ and f in fig. 2.2–2.4 denote the corresponding curves, and the scaled quantities $\rho/2$ and f/f_0 are laid on the vertical axis.

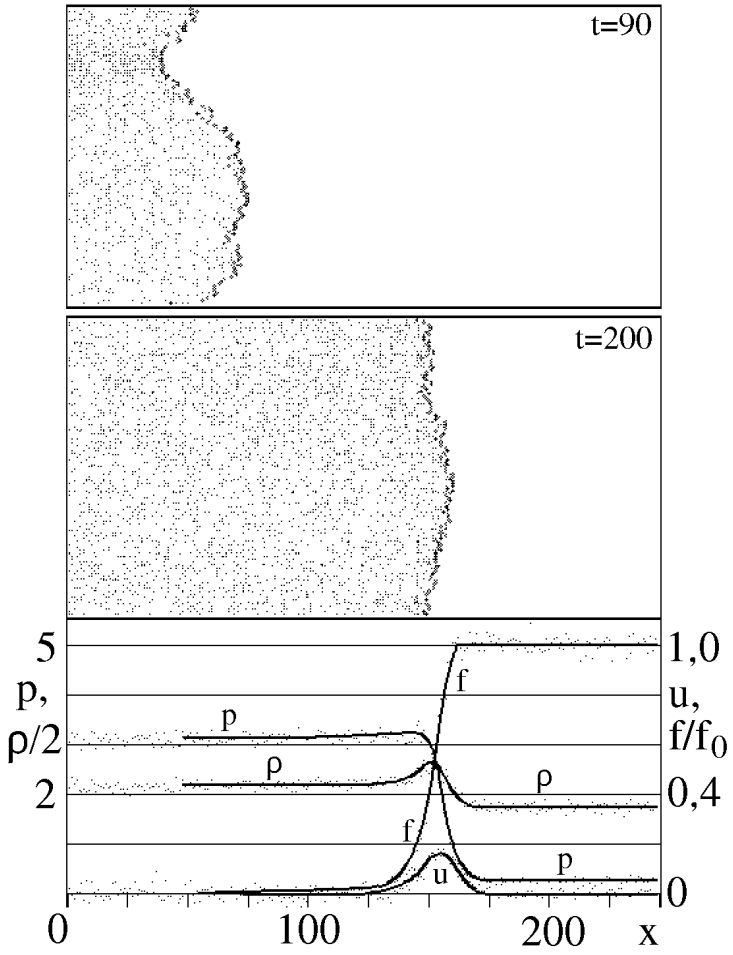

Figure 2.3. Slow wave at low initial temperature

Hence, the wave is supersonic with respect to both the cold initial gas and reaction products. In further computations, we set $w = 0{,}5$.

Figure 2.3 shows the results for a colder initial state with temperature half that used in the previous computations. Here the front is also significantly irregular and the wave velocity is equal to 0.78, which is less than the velocity of sound in the initial state. As a result, there is a certain increase in pressure and velocity ahead of the ignition front. The gas has managed to lead the slow combustion wave. This may be a source of some nonstationarity. The gas ahead of the front favors faster ignition and acceleration of the wave front. However, because of large friction, the penetration effect is slow, and in the computational domain, acceleration was not observed.

2.3 Effect of heat losses

In experiments there is a heat flow from the reaction mixture to the porous bed, which leads to cooling of the gas. Elaboration of the lattice model allows this effect to be taken into account. The scheme is supplemented with a fifth step

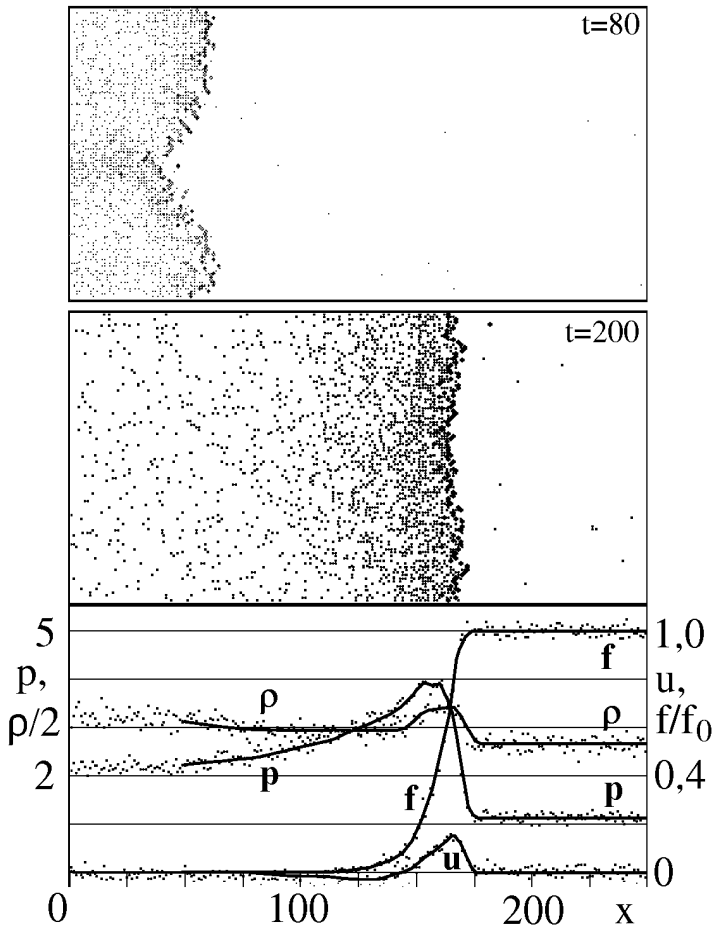

Figure 2.4. Combustion wave in the presence of heat losses

— computation of heat losses. The heat flux (per unit volume of the pores) was calculated from the formula

$$q = \frac{6(1-\varphi)}{d} \cdot \frac{\kappa(T-T_0)}{\varphi d} \cdot \mathrm{Nu},$$

where d is the particle diameter, κ is the thermal conductivity of the gas, T_0 is the initial temperature, and Nu is the Nusselt number. The standard Denton relation was used [85]: $\mathrm{Nu} = 2 + 0{,}6 \cdot (\rho u d\varphi/\eta)^{0{,}7}$, where η is the dynamic viscosity of the gas. At each node, the heat losses q was calculated in dimensionless units. Then, the energy at a node was decreased by two units with probability $q/2$, which simulates the heat loss per unit step in time. The mass and momentum were not affected.

The computation results are shown in fig. 2.4. The initial pressure (1 MPa) and particle size of the porous medium (2.5 mm) are the same as in [75]. In the computation, the initial density was 5.3 kg/m^3 (2.5 times lower than in [75]). The difference in density results from the inaccuracy of the model. It is not significant because the main dependences are easily scaled (the pressure rise, for example, is nearly proportional to density). An exception is heat exchange ($q \sim \rho^{0.7}$, and the energy in unit volume is proportional to ρ). Because of the

decreased density, cooling in the computation is accelerated by approximately 30%, which can be neglected taking into account the qualitative character of the computation model. Thus, the effect of density is also insignificant for heat exchange.

The computed wave velocity (925 m/s) is close to the experimental value (940 m/s). The pressure profile shape is also in qualitative agreement with measurements [75]. The agreement of the pressure rise time suggests a reasonable choice of the kinetics and the agreement of the pressure decrease indicates that the heat exchange was properly taken into account.

We note that the experimental and computed pressures agree only in order of magnitude. This difference is partly related to the lower initial density but even after multiplication of the computed pressure by 2.5 — the ratio of the experimental and computation densities — a difference of about three times remains. This is of course a consequence of the inaccuracy of the model. Because of the discrete nature of the processes and the stiff bounds for the main constants, it is impossible to simultaneously obtain agreement for wave velocity and amplitude.

A better agreement is achieved by correcting the model and recalculating the results using reasonable physical considerations. Let us consider the difference in the properties between the real and lattice gases. The real adiabatic exponent of the combustion products is $\gamma \approx 1.3$, and the energy release per unit mass of the products is $Q \approx 11$ kJ/g. For the lattice model, $\gamma = 2$ and $Q = 1$ kJ/g (in the adopted units). The reaction proceeds in a practically constant volume, and the final pressure is $P \approx (\gamma - 1)\rho Q$. For a real fuel of stoichiometric composition, the final density is $\rho \approx 1.3\rho_0$, and in the computations presented in fig. 2.4, $\rho \approx 1.5\rho_0$. With equal initial density of the oxidizer ρ_0, the model should give a pressure about three times lower than that in the real process.

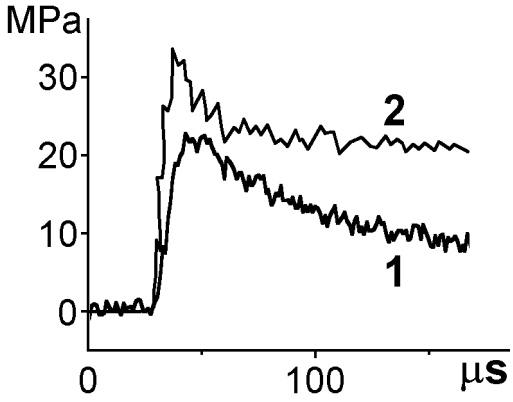

Figure 2.5. Curves of $p(t)$ for the present computation (1) and the experiment of [75] (2)

Figure 2.5 gives curves of pressure versus time. Curve 1, showing the average pressure in a certain cross section, is calculated from the data of fig. 2.4, and curve 2 is an experimental curve taken from [75]. The initial pressure in the computation is subtracted to simulate a piezoelectric gauge record. The computed pressures are increased by a factor of 7.5 to compensate for the differences in thermodynamics and stoichiometry (coefficient 3) and initial density (coeffi-

cient 2.5). After this recalculation, quantitative results of modeling practically coincide with the experiment. We note that the heat exchange is overestimated by approximately 30%, which explains in part faster decrease in computed wave pressure. The residual difference has the same order of magnitude as the experimental scatter. This agreement is even better than one might expect for the model considered. Thus, the comparison performed shows that the lattice model gives a reasonable description of the process.

The computations show a qualitative agreement with the experimental picture of the phenomenon. The wave generally has an irregular front, whose bulges should be identified with the initiating jets. The protrusion at the front where the reaction begins and the pressure increases tends to propagate further. In contrast, friction and lateral expansion of the protrusion stabilize the front. The interaction of the randomness, gas dynamics, and dissipation determines the front shape.

The wave velocity is close to the velocity of sound. The jet mechanism suggests exactly this order of magnitude for the average velocity of the front [86]. However, in wave computation by the continual model, one has to specify the velocity of the front. In the discrete model with specified kinetics, the motion of the front is obtained automatically. This, along with simulation of the complex front shape, is among the unquestionable advantages of the discrete method. We note that supersonic (relative to the products) waves are qualitatively similar to subsonic waves because of friction, which quenches gas-dynamic perturbations [86]. Generally, the regimes obtained can be considered as intermediate between combustion and detonation.

The flow velocity is about an order of magnitude lower than the wave velocity. This, as well as the general wave structure, is in good agreement with the results of the simplified continual model of [86]. We note that in the discrete model, friction is quite real, thus describing the most important feature of the wave — stagnation of average flow. At the level of mechanics, the "short model" [86] is supported by direct computations. The heat exchange in the model is also real (to an extent to which it is possible to use the notion of temperature).

At the same time, the model is rather crude. Because of the small number of energy states, the temperature of the lattice gas is limited (not more than 1). For a more accurate simulation of the large temperature and pressure gradients (by several tens times), one need to assign an initial state with a temperature of about 0.01, i.e., a state that practically consists of rest particles. The physical meaning of such formulation is questionable.

Summary

The lattice method is useful for modeling the mechanics of the process, because, first of all, it takes into account fluctuations and randomness at the mesoscale (pore size). Usually, statistical noise is regarded as a shortcoming of lattice computations but in the present problem it is vital. Waves with a reaction in crowded space is an almost ideal object for the lattice approach.

At the same time, the lattice gas is a qualitative method with respect to kinetics and thermodynamics. At present, however, due to the inaccuracy of available experimental information there is little point in more refined approaches. We believe that there is no ideal computational method and it is most reasonable to combine discrete and continual approaches.

Chapter 3

Simulation of mixing of heterogeneous HE components

The majority on high explosives (HEs) used are blend ones. Properties of components differ that produces interaction on the grain scale (mesoprocesses). Lattice methods are suitable to investigate the hydrodynamic interaction of components.

Mixing of fluids due to their hydrodynamic interaction was so far mainly investigated for sparse systems. Mainly, a flow of one gas or liquid around a bubble or a drop of another gas or liquid was studied [87–90]. Several experiments dealt with a few inclusions, including ones of different size [91,92]. Comparison of theoretical, experimental and computation results was performed in [93].

The typical example of blend HE is the TNT/RDX composition. Here, the concentration of both components is not small (compositions such as TNT/RDX 50/50 are of practical interest). Account of mixing of HE components is particularly important to understand the process of detonation synthesis of diamond.

At high concentration, it is natural to consider a constrained flow, with periodic boundary conditions. From the computation viewpoint, this statement of the problem is even simpler, because the boundary conditions for a single inclusion are nontrivial. As a first approximation, one can consider the flow of one gas around a region of another gas with close density.

Computation of instability development and mixing is rather complicated for traditional finite-difference methods. At the same time, such problems are naturally formulated in the lattice methods, moreover, the unknown boundaries between regions occupied by different substances are obtained automatically. Lattice gas simulations of the Kelvin–Helmholtz instability was performed in [94], of the Rayleigh–Taylor instability — in [94,95]. The LBE method was also used to simulate the Rayleigh–Taylor instability in [72] and to simulate drop

deformation in shear flow in [96].

Experimental indications to the presence of component interaction in detonation products (DP) were obtained at the investigation of electric conductivity. Conductivity of DP of TNT/RDX mixture decreases monotonically with the increase in RDX fraction. Recent experiments showed that conductivity depends not only on the RDX fraction but also on the size of RDX particles [97]. Conductivity of coarse-grained compositions is higher, in some cases by an order of magnitude. Characteristic time of conductivity decrease also grows with increase in particle size. One of the causes of this effect can be mixing of DP of TNT and RDX behind the detonation front [9]. Conductivity of DP of TNT and RDX differ significantly (conductivity of TNT is high due to the release of free carbon), therefore, electric current flows mainly through the connected region consisting of DP of TNT. Amount of pure DP of TNT decreases due to diffusion mixing; hydrodynamic interaction can twist, elongate and break connected conductive region. Both effects should lead to the decrease in conductivity.

The diffusive mixing is effective for small particles only (thickness of the diffusive layer is of order of 2 mkm for 1 mks) [98]. For large particles, one should consider the effect of hydrodynamics and compute emerging flows. Relative velocities u of order of hundreds meters per second can arise in DP due to difference in properties of individual HEs (V.V. Mitrofanov, V.M. Titov [98]). The tangential velocity discontinuity exists at the grain boundaries, and the Kelvin–Helmholtz instabilities develop.

3.1 Diffusion

The effect of molecular diffusion was investigated by the LGA method in two geometries. The model with 9 velocity vectors was used [20] (fig. 1.3). The diffusivity $D = 0.56$ (in lattice units) was determined by the comparison of the numeric and the analytic self-similar solutions for the contact of two half-spaces of different color.

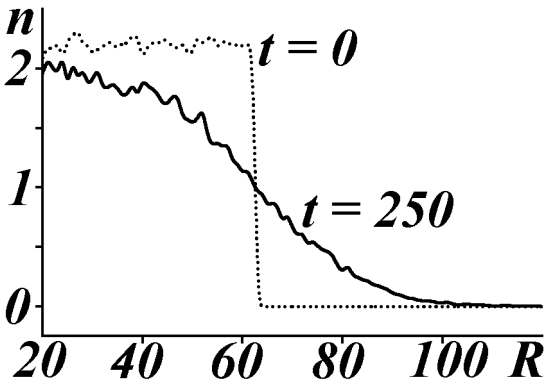

Figure 3.1.

The evolution of the round region of one gas surrounded by another gas is shown in fig. 3.1. Radial dependence of concentration is given for two time instants. If we suppose the drop diameter (125 lattice units) to be 5 mkm, and the diffusivity to be $D = 0.04$ cm^2/s, then 250 time steps correspond to 0.056 mks. Here, the

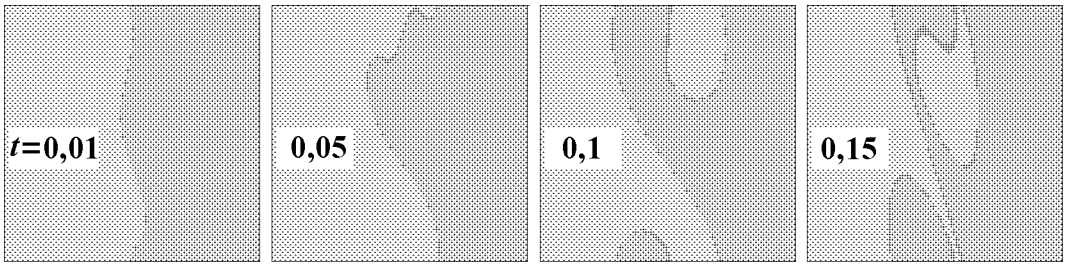

Figure 3.2. Instability of the tangential discontinuity.

diffusion is already significant.

The LGA model is able to take into account diffusion as a physical process, which is a certain advantage. The computation experience showed however that the transition to larger particles and inclusion of hydrodynamic interactions required the unreal increase in the computation scale. The Kelvin–Helmholtz instability was therefore computed by the LBE method which is more flexible. The LBE model on the square grid with 9 possible velocity vectors was used (fig. 1.4,*a*).

3.2 Small-scale instabilities

Figure 3.2 presents an example of such instability (time is in microseconds).

On different sides of the interface, the initial velocity had opposite directions. The interface was given by the equation $x = L/2+3(\cos(2\pi y/L)+\cos(3\pi y/L))$, here $L = 100$ is the size of computation cell. On the top and bottom boundaries, periodic boundary conditions were imposed, and the right and left boundaries were rigid walls without friction. The Reynolds number calculated by the size of the cell was $\mathrm{Re} = 2uL/\nu \approx 500$. The growth of initial perturbations proceeded, then the turnover of wave crests and the formation of vortices. A black layer at the interface is a region were the diffusive mixing is substantial. The recalculation to the physical values gives the size of the cell of about 10 mkm (assuming $\nu = 0.04$ cm^2/s [99], and $u = 200$ m/s). Therefore, these results can be treated as a small-scale "secondary" instability on the drop surface.

3.3 Flow around the cylinder

Figure 3.3 shows the development of the flow of fluid 1 (light region, moves to the right) around the initially round drop of fluid 2 (dark region, moves to the left). In this and following computations of this chapter, both the horizontal and vertical boundary conditions were periodic. The Reynolds number calculated by the drop diameter was about 1530 for fig. 3.3,*a* (size of computation cell

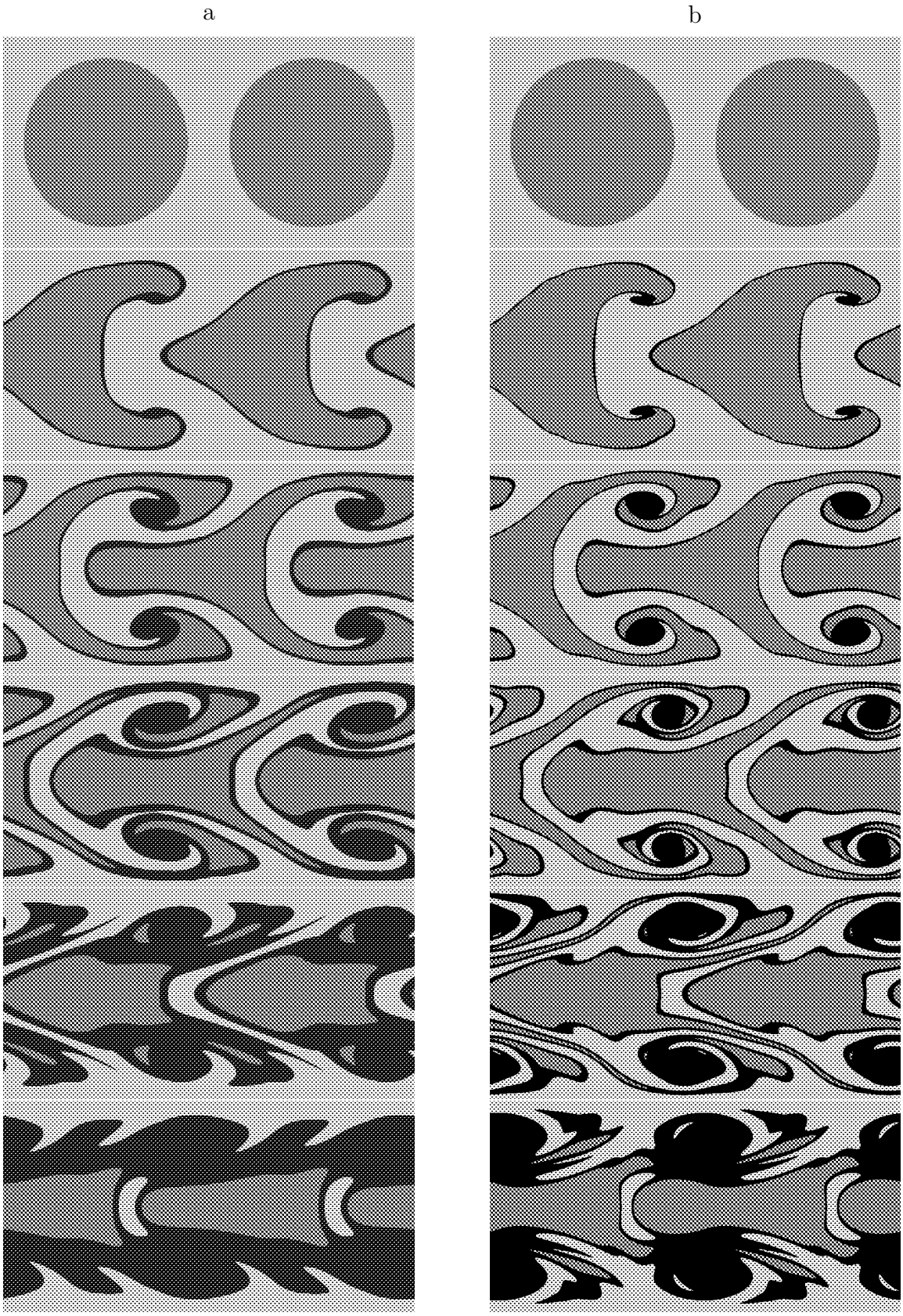

Figure 3.3. Instability development and mixing at the flow around cylinder. Reynolds number $\mathrm{Re} \approx 1530$ (*a*), and $\mathrm{Re} \approx 4900$ (*b*). Time (from top to bottom) $t/t_f = 0$, $t/t_f = 1$, $t/t_f = 2$, $t/t_f = 3$, $t/t_f = 4$, $t/t_f = 5$

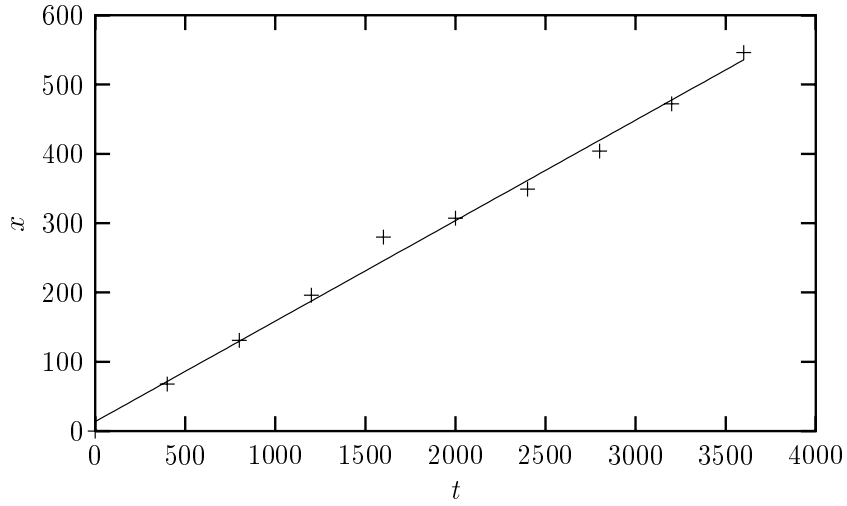

Figure 3.4. Time dependence of the "drop" front point

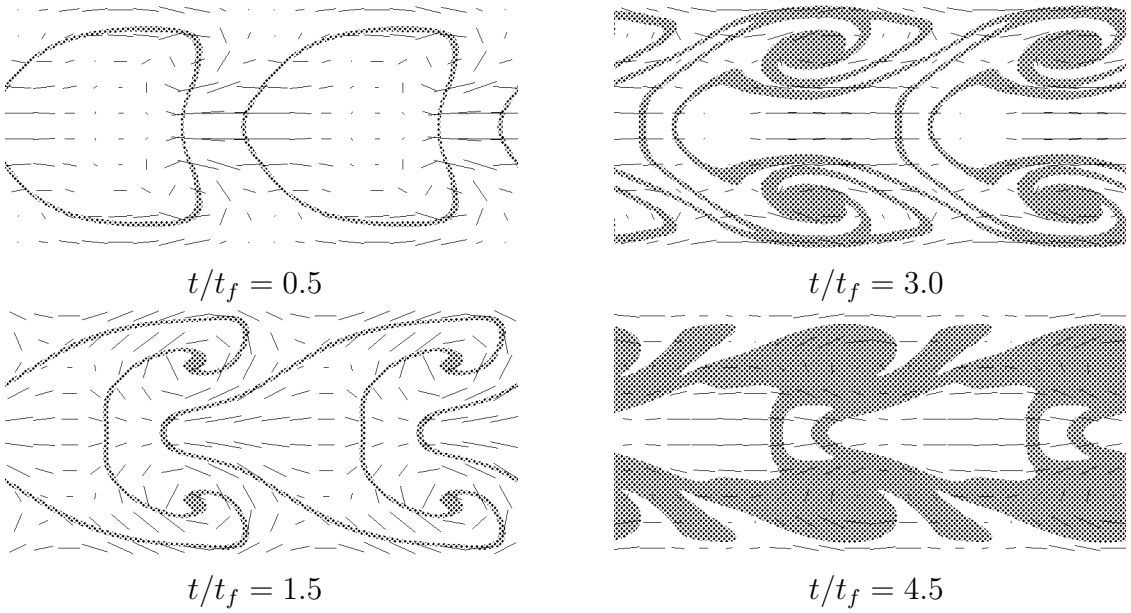

Figure 3.5. Velocity field in the flow around the cylinder. The flow corresponds to the fig. 3.3. The region of diffusive mixing is grayed

was $L = 400$, velocity of drop and surrounding flow was $u = \pm 0.2$, kinematic viscosity was $\nu = 1/12$, drop diameter was $d = L\sqrt{\frac{2}{\pi}}$ — drop occupied half of cell volume) and $\mathrm{Re} \approx 4900$ for fig. 3.3,b (here, the the size of computation cell was doubled, $\nu \approx 0.05$). The characteristic flow time was $t_f = d/2u$. If we suppose $u = 100$ m/s, then $t_f \approx 5d$ mks (d in millimeters).

At the instability development, the boundary elongated and twisted and vortices arose. The region is shown with black, where the absolute value of concentration difference of components $|\rho_1 - \rho_2|$ is less than $0.3\rho_0$. In this zone, a diffusive mixing can be regarded substantial.

It is of interest to consider the motion of the front poind of "drop". Figure

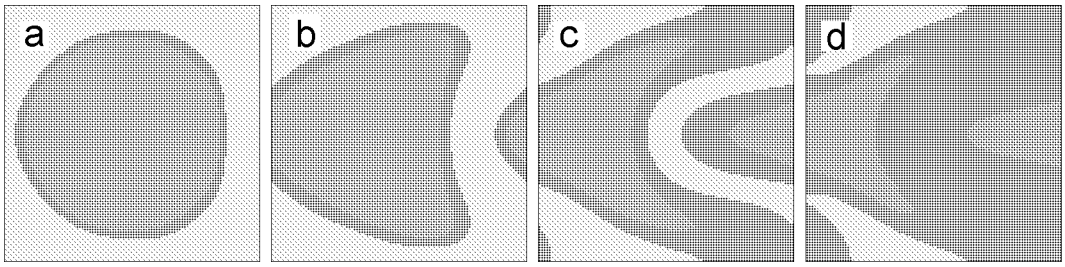

Figure 3.6. Instability development leading to the break of current channels. Dimensionless time $t/t_f = 0.25$ (a), 0.75 (b), 2.0 (c) and 2.75 (d)

3.4 indicates that its velocity remains virtually constant despite the resistance of counter-flow. The average velocity of the drop "nose" calculated by the least-square method was $v \approx 0.145 \pm 0.004$ (strait line in fig. 3.4). This effect is caused with a formation of the flow in the form of a vortex ring (fig. 3.5). Since vortex rings can maintain their individuality for a long time, their formation should lead to the slowing down of the mixing at its later stages.

In the case of smaller particles, the overlapping of tongues of mixed substance is possible (fig. 3.6, here $Re \approx 200$). Clearly, it should lead to sharp decrease in the electric conductivity due to disappearance of the connected net of conducting channels.

3.4 Effect of the initial system geometry

In the real TNT/RDX "alloy", RDX particles are not round. Rather, grains are polyhedral. Therefore, the influence of peculiarities of the shape of initial inclusionx on the hydrodynamic interaction of components is of interest. Figure 3.7 presents different stages of instability development in the flow around initially square "drops" with different initial orientation relatively to the flow. The process is in general similar to the fig. 3.3, but the mixing is faster due to the presence of corners, at which instabilities develop faster.

In all computations above, drops were initially placed at nodes of a simple square lattice. It is of interest to investigate the change of mixing pattern for the initial layout with different symmetry.

In the next series of computations, the initial drop layout was diagonal (the square lattice, rotated by 45° over the relative velocity vector — the "checkerboard" layout). That is, the coordinates of a center of one round drop were (0,0) (this drop appears as four regions in the corners of the computation cell because of periodic boundary conditions). Another drop was placed in the center of cell. The computations were also carried out, with one drop sub-system shifted rel-

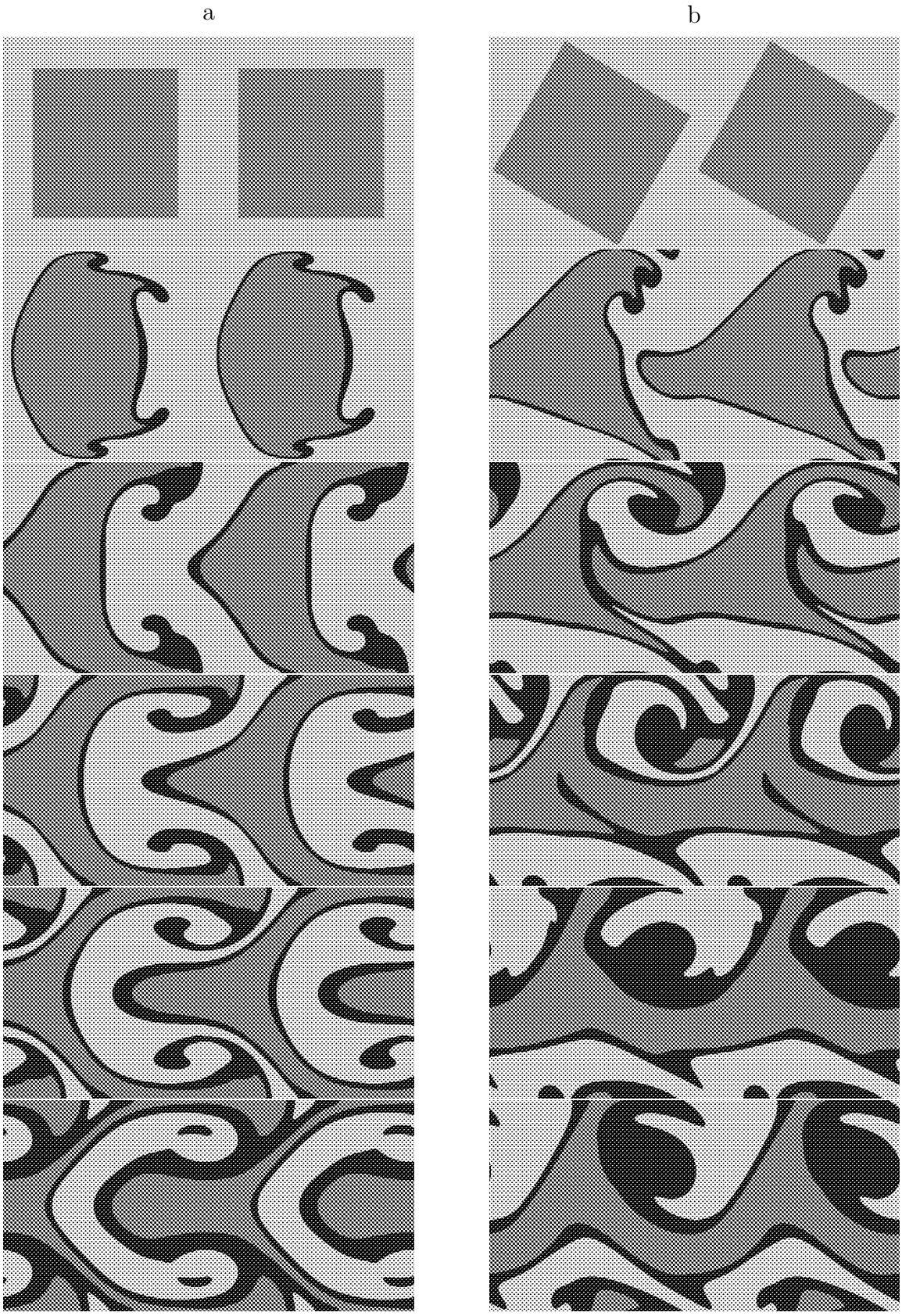

Figure 3.7. Instability development and mixing at the flow around square. Reynolds number is Re ≈ 800. Time (from top to bottom) $t/t_f = 0$, $t/t_f = 1$, $t/t_f = 2$, $t/t_f = 3$, $t/t_f = 4$, $t/t_f = 5$. Square was initially perpendicular to the flow (a) and rotated by 30° (b)

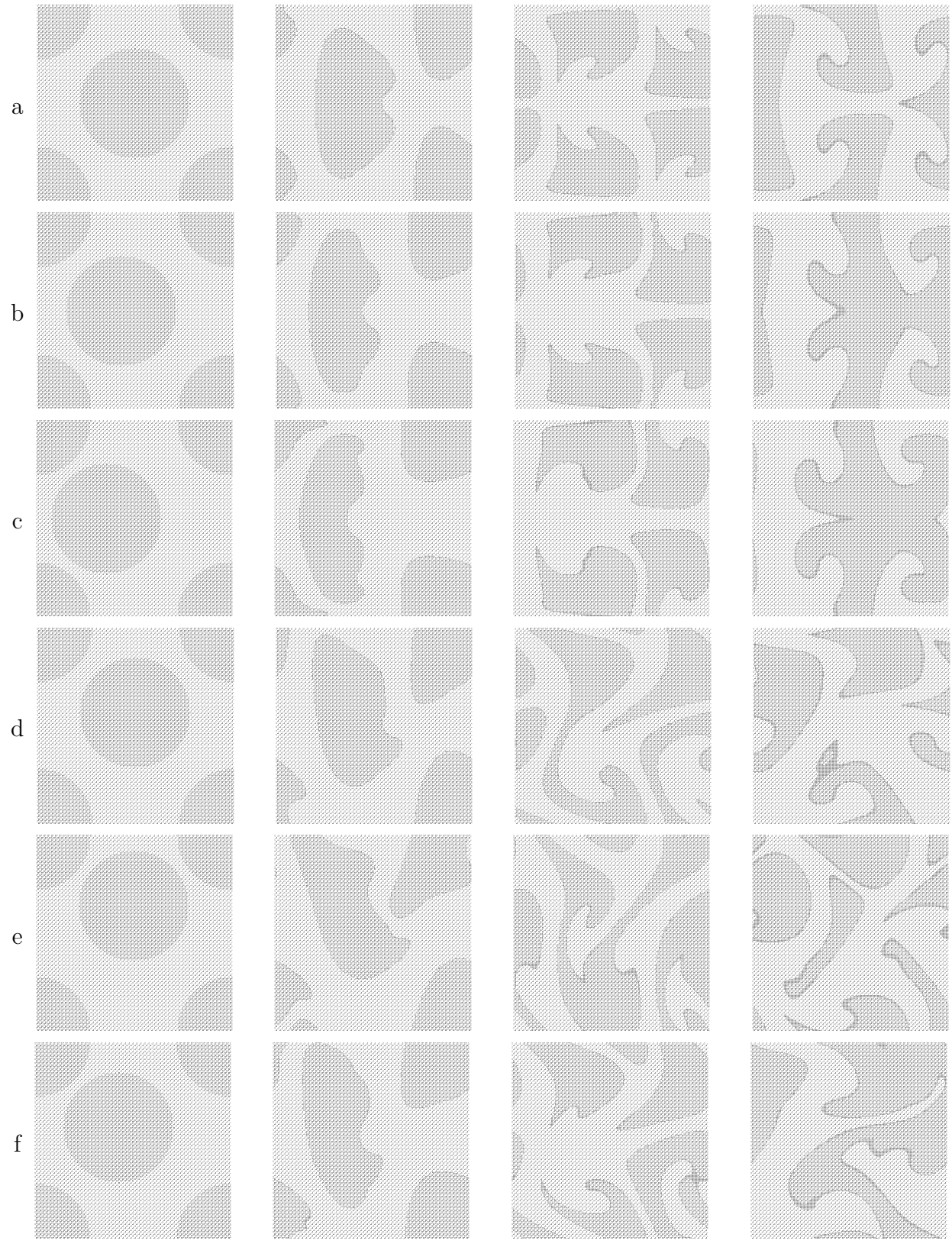

Figure 3.8. Flow for the "diagonal" drop layout. Displacement of the central cylinder is *a*: $(\Delta x, \Delta y) = (0, 0)$, *b*: $(\Delta x, \Delta y) = (-d/8, 0)$, *c*: $(\Delta x, \Delta y) = (-d/4, 0)$, *d*: $(\Delta x, \Delta y) = (0, d/8)$, *e*: $(\Delta x, \Delta y) = (0, d/4)$, *f*: $(\Delta x, \Delta y) = (-d/8, d/8)$

ative to another one in horizontal or vertical direction (this was attained by the shift of the central drop). In all computations, the size of computation cell was $L = 200$, the flow velocity was $u = 0.2$, the kinematic viscosity was $\nu = 1/12$, the drop diameter was $d = L/\sqrt{\pi} \approx 112$, the characteristic flow time was $t_f \approx 280$, and the Reynolds number was $\mathrm{Re} \approx 540$). Development of instabilities for different initial layouts is presented in fig. 3.8. For all series, the first frame corresponds to $t/t_f = 0$, the second one to $t/t_f = 1$, the third one to $t/t_f = 3$, and the fourth one to $t/t_f = 5$.

The flow pattern for the "checkerboard" initial layout of inclusions differs appreciably from the case of the simple lattice. The flow changed rapidly from the mainly horizontal one to the mainly vertical flow with a system of vortices. A substantial deformation of drops occured, with their fragmentation and merging of fragments at later stages. In some cases, a blocking of the cell with on of the direction happened (e.g., fig. 3.8,b,c,e,f).

3.5 Mixing due to the pulse acceleration

The velocity discontinuity may arise as a result of the passage of shock waves through the interface of fluids with different density (Richtmyer–Meshkov instability, RM) or the acceleration of the medium which is analogous to the action of gravitation (Rayleigh–Taylor instability, RT). RT instability corresponds to the constant acceleration, for the RM instability, time dependence of acceleration is given by δ-function.

In this work, an intermediate case was considered — horizontal acceleration was $a = a_0$ at the time interval $0 \le t \le t_f$, later, acceleration turned zero. Characteristic flow time was $t_f = d/2u$, the value of acceleration was chosen so as $a_0 = u/t_f$. Size of computation cell was $L = 400$, velocity $u = 0.2$, cylinder initially occupied half of the cell.

The action of forces on the substance was calculated in the Boussinesq approximation: the force acting on the substance at a node $\mathbf{x}$ is $\mathbf{F}(\mathbf{x}) = \mathbf{a}(\rho_1(\mathbf{x}) - \rho_2(\mathbf{x}))$. Development of instability is presented in fig. 3.9. Density distribution during the mixing process is similar to the case presented in fig. 3.3. This fact justifies the simplified formulation used in sections 3.2–3.4.

3.6 Computation of the electric conductivity

The electrical conductivity of the cell was computed based on the hydrodynamic configurations obtained using the relaxation method. The electric potential

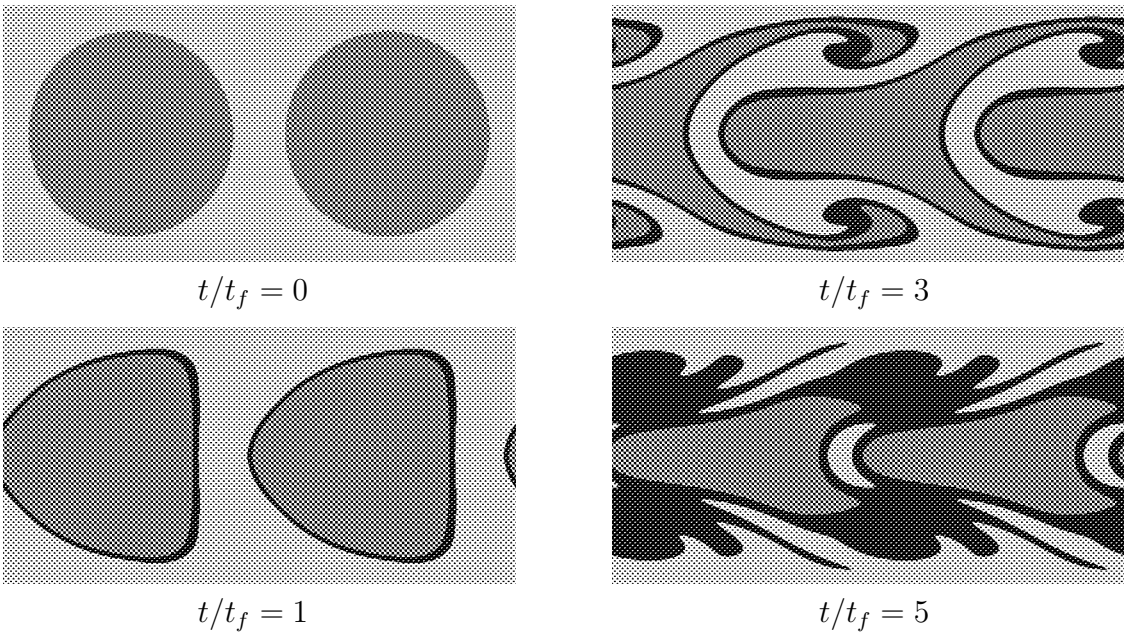

Figure 3.9. Mixing due to the Raylegh–Taylor instability

was specified at the opposite edges of the cell ($\varphi = 0$ at one edge, $\varphi = \varphi_0$ at the opposite one) and the conductivity of each lattice link was calculated as $Y_{ij} = \sigma_0 h \sqrt{n_i n_j}$. Here, σ_0 is a constant, n_i, n_j are the "effective concentrations" of the conductive phase at terminal nodes of a link ($n = \max(\rho_{TNT} - \rho_{RDX}, 0)$), h is the lattice spacing. This formula reflects both the "dilution" of highly conductive DP of TNT and the "poisoning" of the conductivity at the mixing (which can result from secondary chemical reactions between DP of TNT and RDX leading, e.g., to the burning of free carbon). Then, the equations of conductive charge transfer

$$\partial q/\partial t = -\mathrm{div}\ \mathbf{j} = -\mathrm{div}(\sigma \mathbf{E})$$

were solved along with the Poisson's equation for the electric potential $\Delta\varphi = -4\pi q$ using the time-implicit scheme of [100]. The changes of node charges Δq_i were calculated using the potential values obtained. Calculations continued until the maximum change $|\Delta q_i|$ became lower than a specified value. Then, the current through the cell was calculated as $I = \sum\limits_i Y_{i0} \Delta\varphi_i$, where the summation was over a layer adjacent to one of the edges with fixed potential. The cell conductivity $Y_x = I_x/\varphi_0$ was computed in the horizontal direction, $Y_y = I_y/\varphi_0$ — in the vertical one. In following graphs, the averaged value $\langle Y \rangle = (Y_x + Y_y)/2$ is shown.

Several computations of time dependence of the electric conductivity were performed for different drop diameters d. The results are presented in fig. 3.10. The time of the conductivity decrease increases with the enlargement of the

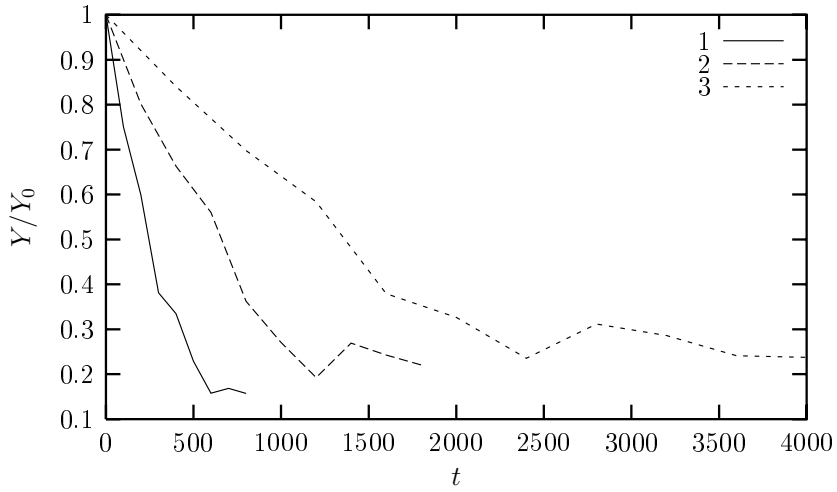

Figure 3.10. Time dependence of the electric conductivity. 1 — $d = 80$, 2 — $d = 160$, 3 — $d = 320$

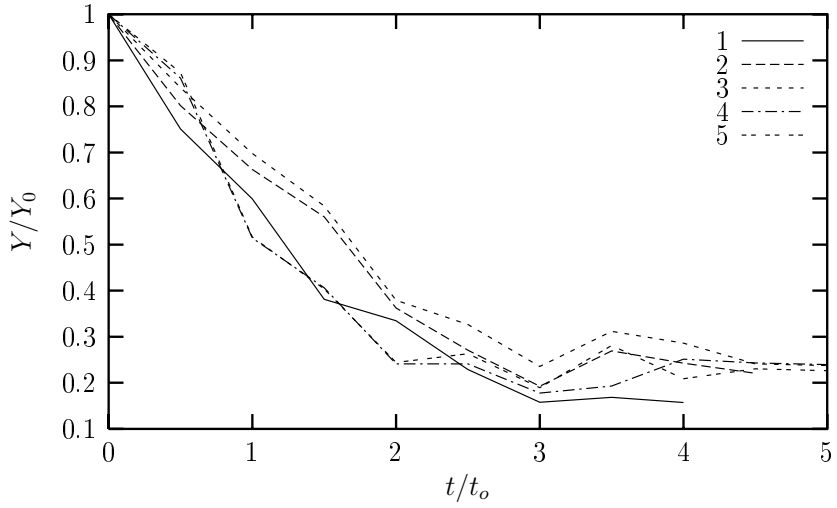

Figure 3.11. The dependence of the electric conductivity on the dimensionless time t/t_f. 1 — $Re \approx 400$, 2 — $Re \approx 800$, 3 — $Re \approx 1600$, 4 — $Re \approx 2550$, 5 — $Re \approx 4900$

drop size, therefore the average value of conductivity is greater for the coarse-grain medium, in agreement with experimental results of [97].

The dependence of conductivity on the dimensionless time t/t_f for different Reynolds numbers is also presented in fig. 3.11. Graphs virtually coincide, thus, the mixing is virtually self-similar.

Figure 3.12 presents time dependencies of the conductivity for inclusions of different shape. The cell conductivity decreases faster for square inclusions than for round ones, although graphs are qualitatively close.

Figure 3.13 presents the time dependence of the cell conductivity for the diagonal initial drop layout (curve 1, corresponds to fig. 3.8,*a*), for the horizontal shift of one sub-system of cylinders by $\Delta x = -d/4$ (curve 2, corresponds to fig. 3.8,*c*), for the vertical shift by $\Delta y = d/4$ (curve 3, corresponds to fig. 3.8,*e*),

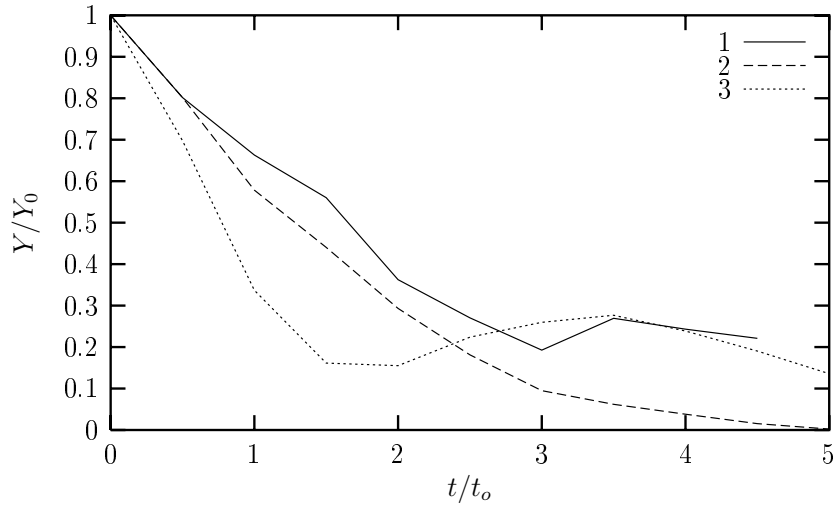

Figure 3.12. The dependence of the electric conductivity on the dimensionless time t/t_f for different drop shape. 1 — cylinder (fig. 3.3,), 2 — square (fig. 3.7,*a*), 3 — slanted square (fig. 3.7,*b*). In all cases $Re \approx 800$

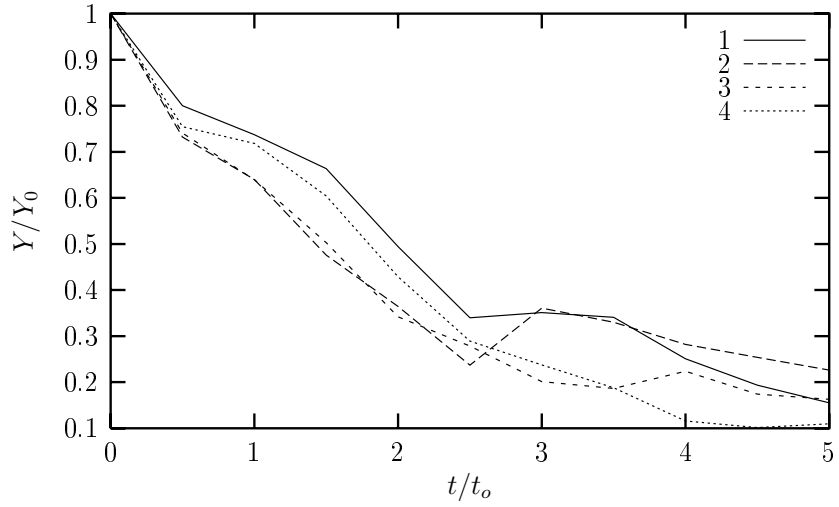

Figure 3.13. The dependence of the electric conductivity on the dimensionless time t/t_f for diagonal drop layout. 1 — see fig. 3.8,*a*, 2 — see fig. 3.8,*c*, 3 — see fig. 3.8,*e*, 4 — see fig. 3.8,*f*

and for both the horizontal and vertical shift by $\Delta x = -d/8, \Delta y = d/8$ (curve 4, corresponds to fig. 3.8,*f*). Conductivity decrease for "shifted" layouts is faster, although graphs are close.

Characteristic time of conductivity decrease by e times was $\tau \approx 2t_f$ in all cases. For drops of 200 mkm it gives 2 mks, with quite good agreement with experiments [97]. The value of decrease time for millimeter particles (10 mks) is sufficiently greater than experimental one. However, it is necessary to take into consideration that the mixing is not the only process leading to the decrease in conductivity. For example, in pure TNT $\tau \approx 1.9$ mks. One can believe, that the conductivity decrease is mainly due to the diffusive mixing for fine-

disperse compositions, whereas hydrodynamic instabilities play the main role for compositions with medium grain size, and expansion of DP makes the major contribution for the coarse-grained ones. Taking into account this remark, we can claim the satisfactory explanation of the experimental data.

Summary

The simulation results of the interaction between detonation products of heterogeneous HEs show the essential role of hydrodynamic instabilities. The computation results agree in general with known isotope date [98], and with the measurements of the electric conductivity [97]. For the micron size of heterogeneity, the diffusion mixing over sub-microsecond intervals is substantial. For the millimeter grain size, the mixing is low, and for regular RDX size of $\approx$ 200 mkm, the extent of the mixing due to the hydrodynamic interaction during some microseconds can be estimated as substantial.

Chapter 4

Simulation of electrohydrodynamic flows

Electrohydrodynamics is a wide class of phenomena in liquids and gases placed in electric field in contact with electrodes. On the electrode surface, charge injection and various electrochemical reactions can occur (later ones can also happen in the bulk of fluid). The electric field exerts a force on the charged particles, at the same time, electric charge changes the spatial distribution of the electric potential. Electrodynamic forces can produce flows of fluid, these flows lead to charge transport.

The breakdown of dielectrics occurs at sufficiently high electric field strength. The breakdown proceeds in several stages. At first, one or several luminous formations appear near one of electrodes. The time between the voltage application and the appearance of such formations is called the statistical lag time, it can be different in subsequent experiments. Depending on conditions, different mechanisms of the breakdown inception are possible: the bubble mechanism, the thermal one, the ionization one, etc.

At the next stage of breakdown, conductive channels (called streamers) grow from the formations appeared to the opposite electrode. Streamers have usually a dendrite-like shape and they can also branch. Patterns of streamer structure are stochastic enough and the structure is not reproduced exactly in subsequent experiments. The electric conductivity inside streamers is sufficiently high, hence, the energy is released there leading to expansion of streamers. Divergent shock waves and flows of liquid arise around each expanding channel. Waves from different streamer channels interact, that additionally complicates the flow pattern. The back-influence of compression waves upon the dynamics of streamer channels is also possible.

When one of streamers reaches the opposite electrode, the last stage of the electric discharge in liquid — the channel one — begins. The energy is released

at the passing of the electric current, the channel expands generating a divergent shock wave. A flux of fluid into the channel through its boundary exists, this fluid is converted to the channel plasma after dissociation and ionization.

Simulation of electrohydrodynamic flows is a complicated problem where one should take into account many concurrent phenomena. In this chapter, flows at a low electric field and the bubble generation near electrodes are considered. Streamer dynamics and flows at the channel stage of electric discharge are considered in chapter 5.

The LBE method with 9 possible velocity vectors on a square lattice ($|c_k| =$ 0, 1 and $\sqrt{2}$) was used in computations of this chapter. To simulate EHD flows, one should incorporate properly the electrohydrodynamic effects [8]:

1. Convective charge transport by moving liquid;
2. Charge transport by conductivity currents, the computation of the electric potential is necessary;
3. Effect of the electrodynamic forces on charged liquid being in electric field.

4.1 Computation of charge transport

The electric charge in a node is changed due to the convective transport of charge by moving liquid and due to the conductivity currents (electric drift of electrons and ions). Below, these mechanisms are considered separately.

4.1.1 Convective charge transport

Equation of the convective charge transport follows from the charge conservation law. This equation is given by:

$$\partial q/\partial t = -\mathrm{div}(q\mathbf{u}).$$

Here q is the charge density, $\mathbf{u}$ is the velocity of liquid. Three methods were used to solve this equation: the method of "LBE-particles", the method of mean velocity and the method of additional LBE component.

In the method of "LBE-particles", the part of node charge $q_k = qN_k/\rho$ is passively transported to the neighbor node along the k-th lattice link. This method results in numeric diffusivity of $D_1 = c_s^2\Delta t/2$. In particular, for the two-dimensional model with 9 directions, one obtains $c_s = h/\sqrt{3}\Delta t$ and $D_1 = h^2/6\Delta t$.

Example of computations is shown in fig. 4.1. There were initial density discontinuity in the middle of the computation cell, the liquid velocity was initially

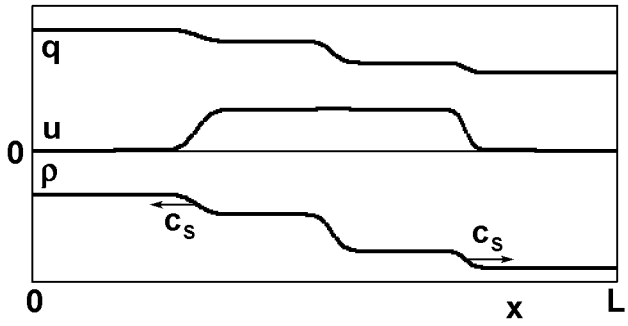

Figure 4.1. Liquid flow and charge distribution at zero conductivity in the absence of electrodynamic forces

zero. The initial charge density was everywhere proportional to the liquid density. The decay of discontinuity occured, a shock wave and a rarefaction wave were generated. The charge distribution coincides with the density distribution (charge is "frozen" into the liquid).

This method is clearly unacceptable for uniform liquid, however, it can be used to compute the dynamics of conductive inclusions, if in two-component medium only one component can carry electric charge.

The method of mean velocity is based on finite-difference method. For the one-dimensional case, the equations are given by:

$$\frac{q^{n+1}-q^n}{\Delta t} = \frac{1}{2h}\left(q^n_{i-1}(u_{i-1/2}+|u_{i-1/2}|) - q^n_{i+1}(u_{i+1/2}-|u_{i+1/2}|)\right.$$
$$\left. -q^n_i(u_{i+1/2}+|u_{i+1/2}|+u_{i-1/2}-|u_{i-1/2}|)\right),$$

where $u_{i+1/2} = (u_i + u_{i+1})/2$. The numeric diffusivity for this method is $D_2 = \frac{|u|(h/\Delta t - |u|)}{2}$, it depends on flow velocity. Maximum of diffusivity is $D_2|_{max} = h^2/8\Delta t$ for $u_m = h/2\Delta t$, it is lower than D_1. A flow velocity is usually much lower than u_m, it additionally diminishes D_2 comparing to $D_2|_{max}$.

The formulas for diffusivity of both methods were tested for the case of a one-dimensional liquid flow with constant velocity u_0 by comparison of numerical results with the well-known exact solution for the diffusion equation

$$q(x) = \frac{Q}{\sqrt{4\pi Dt}} \exp\left(-\frac{(x-u_0 t)^2}{4Dt}\right)$$

with the charge Q initially located at the point $x = 0$. For all velocities within the stability range of the LBE method, the numerical results coincided completely with the exact solution.

In the method of additional LBE component, the charge transport is simulated as the transport of passive scalar (see chapter 1). In this case, the charge diffusivity is $D_3 = \frac{h^2}{3\Delta t^2}(\tau_n - \frac{\Delta t}{2})$, it depends on the relaxation time τ_n, and it can be chosen independent on the properties of liquid.

Test computations were carried out of the liquid flow with charge transfer for different values of charge diffusivity D_3. Results are shown in fig. 4.2.

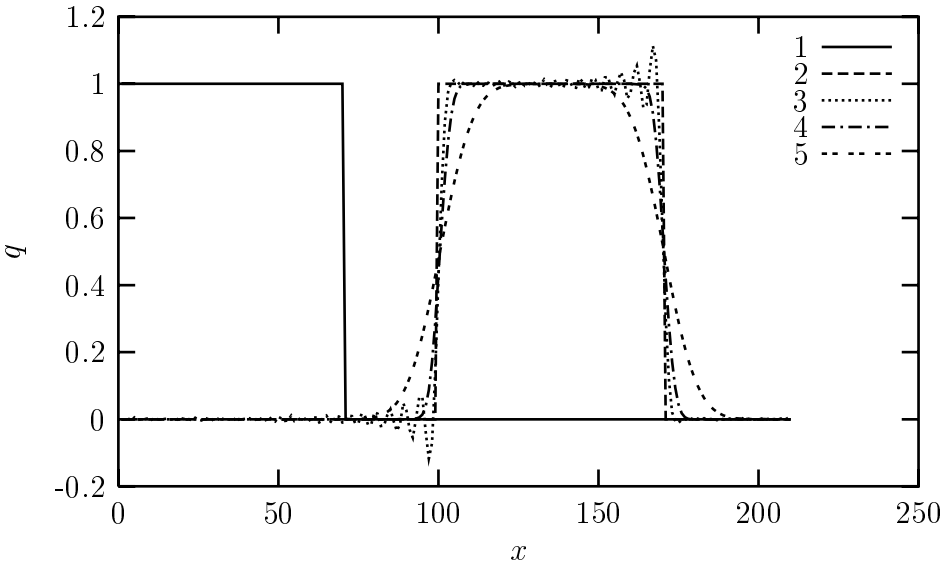

Figure 4.2. Transformation of charge distribution in one-dimensional liquid flow in the case of zero electric conductivity. The velocity of uniform flow was $u_0 = 0.1$. Initial charge distribution (curve *1*); theoretical charge distribution without diffusion (*2*) at $t = 1000$. Computed charge distribution at $t = 1000$ for the diffusivity $D_3 = 3.3(3) \cdot 10^{-4}$ (*3*); $D_3 = 3.3(3) \cdot 10^{-3}$ (*4*) and $D_3 = 3.3(3) \cdot 10^{-2}$ (*5*)

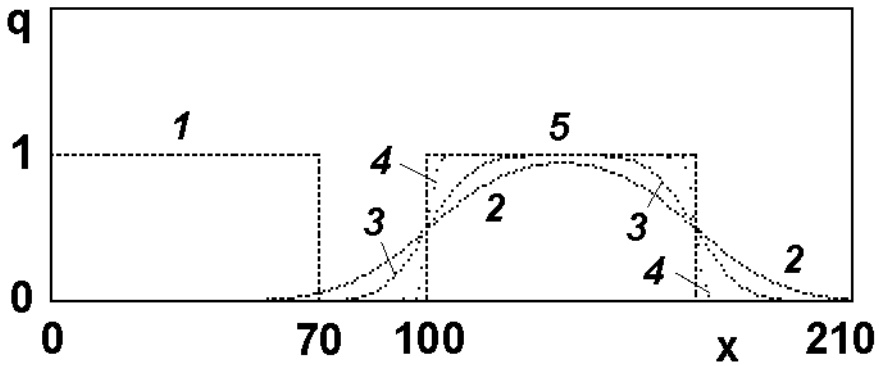

Figure 4.3. Transformation of charge distribution in uniform liquid flow in the case of zero electric conductivity

Electric charge was initially uniformly distributed $q(x) = q_0$ in a region $x_1 < x < x_2$. The liquid flow was uniform with constant velocity $u = u_0$ equal to 0.1. Boundary conditions were periodic. The good agreement with theoretical distribution is clear. At too low values of D_3, oscillations of charge density were observed in regions of high gradients (fig. 4.2, curve 3).

Results of computation of the convective charge transport are shown in fig. 4.3, here the initial and boundary conditions are the same as in fig. 4.2. Curve 1 presents the initial charge distribution. Computation results for the method of "LBE-particles" (curve 2), the method of mean velocity(curve 3) and the method of additional LBE component (curve 4), all for $t = 1000$, are

also shown. Curve 5 is the theoretical charge distribution without diffusion for $t = 1000$. Diffusivities were $D_1 = h^2/6\Delta t$ for the method of "LBE-particles", $D_2 = 0{,}045h^2/\Delta t$ for the method of mean velocity, and $D_3 = 0{,}0033h^2/\Delta t$ for the method of additional LBE component.

Thus, the method of the additional LBE-component allows one to reduce numeric diffusivity by more than order of magnitude comparing with previous methods.

4.1.2 Conductivity currents

The equation of conductive charge transport $\partial q/\partial t = -\mathrm{div}\,\mathbf{j} = -\mathrm{div}(\sigma\mathbf{E})$ was solved together with Poisson's equation for the electric potential $\Delta\varphi = -4\pi q$ by time-implicit finite-difference scheme of [100]. The conduction of each bond was calculated using the expression $G_{ij} = \sigma_0 h\sqrt{n_i n_j}$, where σ_0 is the liquid conductivity, n_i, n_j are the concentrations of the conductive phase at the edges of the bond, h is the lattice unit. This expression ensures electric charge transfer by current only inside the region occupied by the conductive phase. The conductivity of liquids used in EHD apparatuses is usually small. Moreover, it was shown in [101] that in the planar case the charge drift is negligible comparing to the convective charge transport. Therefore, bulk liquid conductivity was assumed zero in following computations. To simulate charge injection, certain conductivity was assigned at layers adjacent to electrodes.

4.2 Electrodynamic forces

Along with charge transfer, the action of electrodynamic forces on a liquid should be taken into account (just these forces are the cause of flow onset). The electrodynamic force acting on the electric charge q at a node is given by $\mathbf{F} = q\mathbf{E} = -q\nabla\varphi$. In the finite-difference form, the cartesian components of the force are $F_x = -q(\varphi_{i+1,j} - \varphi_{i-1,j})/2h$, $F_y = -q(\varphi_{i,j+1} - \varphi_{i,j-1})/2h$. Use of the centered form for the derivative eliminates the contribution of the node charge to the electric field (i.e., the self-action of charge). The action of the electrodynamic force leads to a change of momentum at a node by $\Delta\mathbf{p} = \mathbf{F}\Delta t$, corresponding velocity change is $\Delta\mathbf{u} = \Delta\mathbf{p}/\rho$. The modified velocity was used in the collision operator of the LBE method (equilibrium distribution functions are computed based on the velocity $\mathbf{u}' = \mathbf{u} + \Delta\mathbf{u}$). Thus, the action of the electric field on a charged liquid is computed.

Computation results of one-dimensional liquid flow are presented in fig. 4.4. The liquid flow was simulated by the LBE on a square lattice with 4 values of

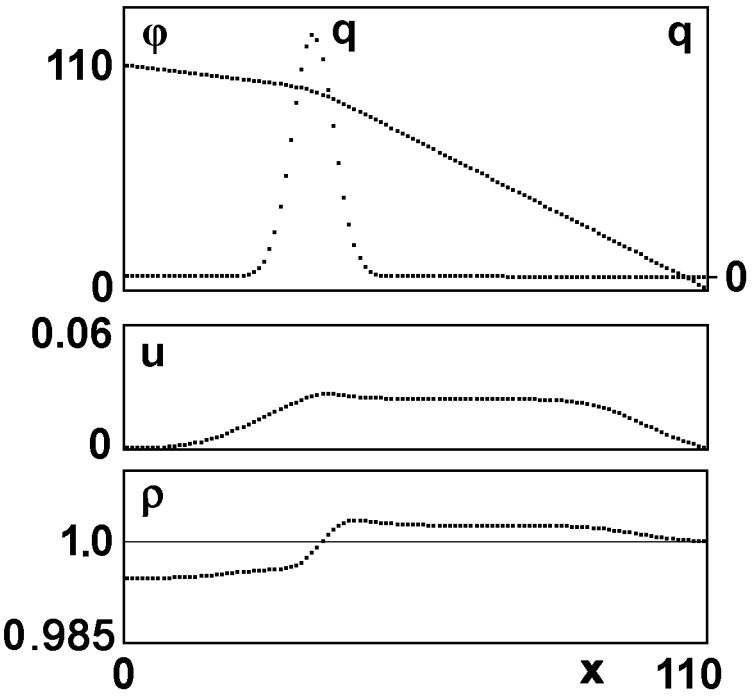

Figure 4.4. Liquid flow and charge distribution. $\varphi_0 = 110$, $Q = 0.08$, $x_0 = 36$, $L = 110$, $t = 70$, $\rho_0 = 1$

velocity (see. fig. 1.4,*b*). The positive charge Q was initially distributed along X coordinate according to the function

$$q(x) = \frac{Q}{\sqrt{2\pi b^2}} \exp\left(-\frac{(x - x_0)^2}{2b^2}\right),$$

charge density was constant along vertical lines. Boundary conditions for Poisson's equation were $\varphi = 0$ at $x = L$, $\varphi = \varphi_0$ at $x = 0$. Left and right boundaries were rigid walls. The charge began to move to the right under the action of electric field, generating the rarefaction wave moving to the left, and the compression wave moving to the right. At the time instance presented in the figure, the rarefaction wave had already reflected from the left wall.

4.3 Two-dimensional EHD flow (EHD-pump)

The EHD flow in two dimensional blade–plane geometry was considered. Computations were carried out in a square cell of size of 106×106 lattice sites between two plane electrodes at the top and bottom. Boundary conditions along the X axis were periodic. The electric potential of the upper electrode was zero, of the lower one it was $\varphi_0 = 106$, hence, the average field in the region was $E_a = 1$. In the middle of the lower electrode, a rectangular protrusion was placed of size of 5×2. The charge injection was possible from the top of the protrusion (conductivity of adjacent liquid layer was $\sigma_0 = 2 \cdot 10^{-4}$).

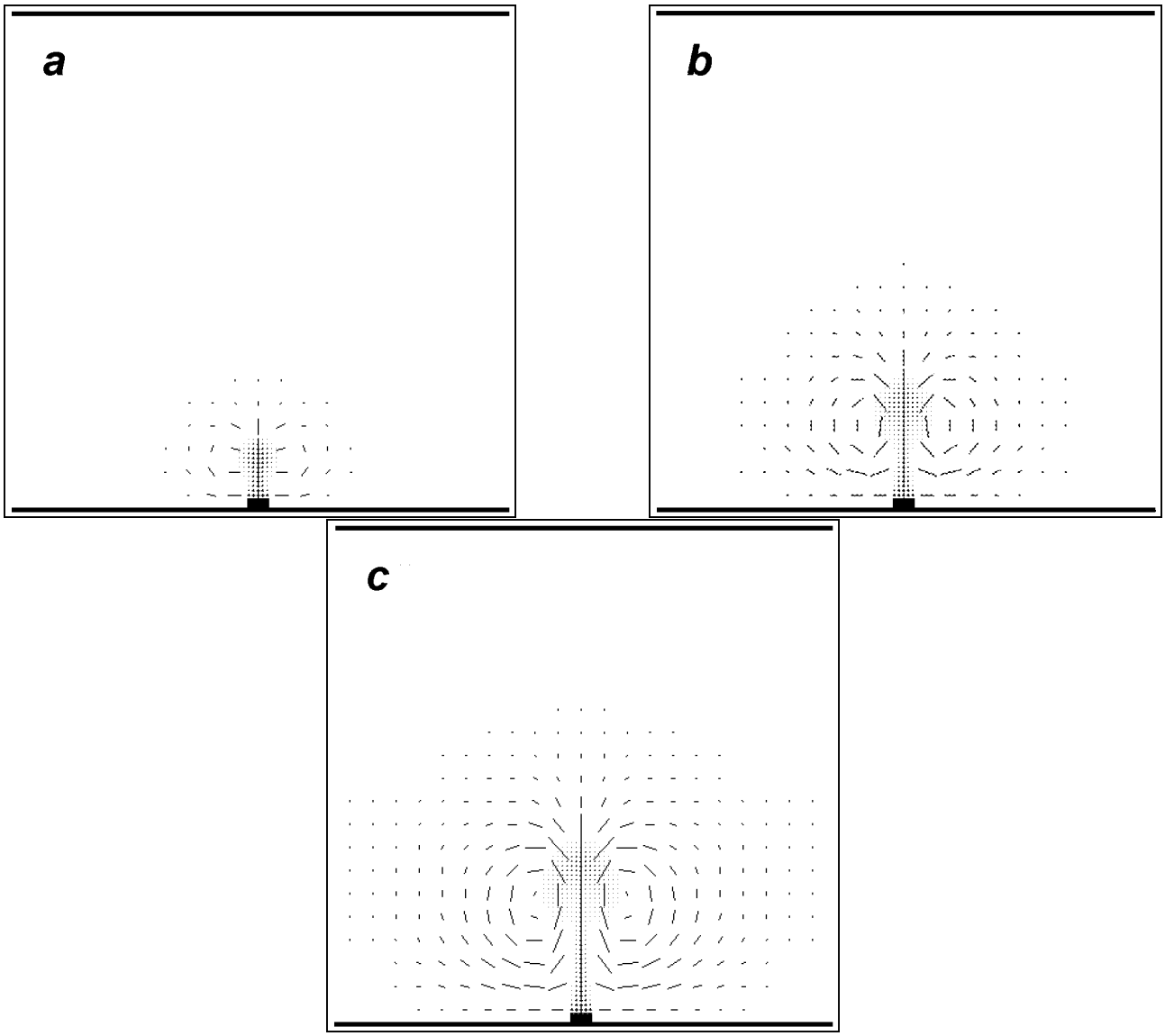

Figure 4.5. Two-dimensional EHD low. Velocity field (shown by lines) and charge density (shown by shades of gray). Time is $t = 275$ (a), $t = 400$ (b), $t = 510$ (c)

Figure 4.5 shows the flow development. When the voltage was applied, the charge injection began from the protrusion. Then a charged lump began to move upwards due to the action of electric field. The liquid flow in the form of vortical dipole was formed. The extent of region of moving liquid and the velocity magnitude grew in time. The maximal velocity in computations was about 0.05. Because of the increase in the "head" of the charged jet, the electric field on the top of the protrusion decreased and further injection was reduced. Development of conductive structures of such type was observed in experiments on the breakdown of highly viscous dielectrics [102], and at certain regimes of the partial breakdown [103].

In this example, no charge sink existed, hence, charge accumulation and flow

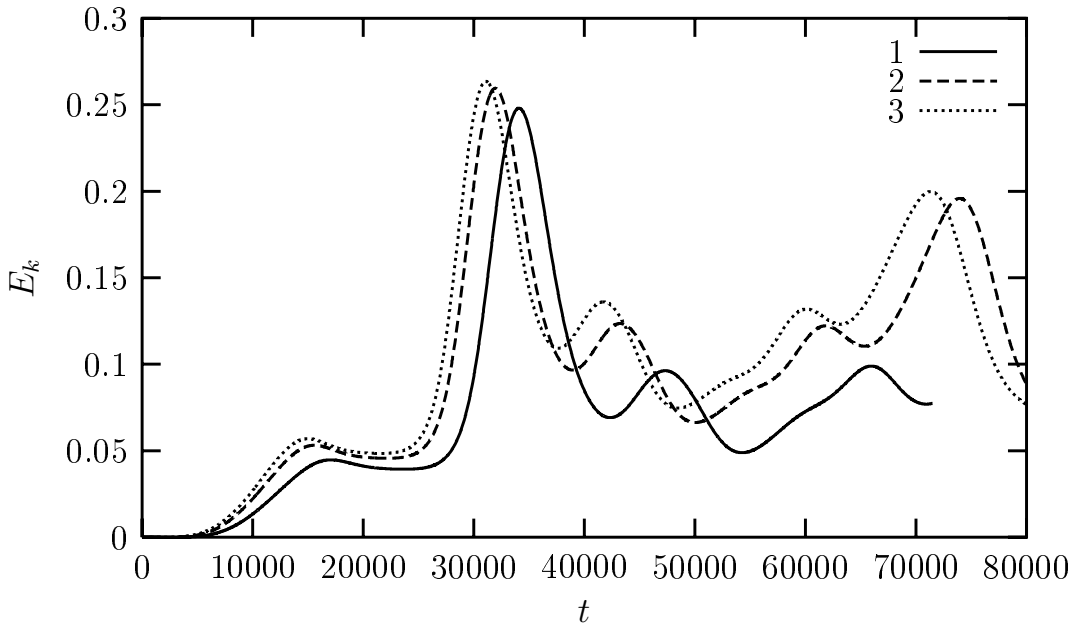

Figure 4.6. Time dependence of flow kinetic energy E_k. 1 — $\sigma_0 = 10^{-4}$, 2 — $\sigma_0 = 2 \cdot 10^{-4}$, 3 — $\sigma_0 = 3 \cdot 10^{-4}$

cessation should occur later. In the next computation, in the same geometry, a conducting layer existed also near the upper electrode with the same conductivity σ_0 as the layer near the blade. Hence, the charge sink existed, and the flow would reach the steady-state regime. Here, a jet of liquid with charge of one sign was observed which ascended from the protrusion along with two oppositely charged descending jets at the vertical borders of the cell. Since the horizontal periodicity, these jets are two parts of one descending jet. The flow between jets consisted of two vortices with opposite signs.

Time evolution of the flow kinetic energy E_k for different values of σ_0 is shown in fig. 4.6. Flow pulsations are readily observable. The cause of them is, that the charge injection leads to the decrease in the electric field on the top of the protrusion thus decreasing the current. When the injected charge moves away from the protrusion, the screening diminishes and the current rises again. Thus, the charge is injected in discrete lumps that are later extended due to liquid motion.

If the voltage between electrodes increases, the main mode of flow becomes unstable. It leads to the growth of small disturbances and the breaking of flow symmetry. Jets shift and distort, additional vortices appear. Figure 4.7 presents the velocity field and the charge distribution at the late stage of flow development. One can readily see complicated flow pattern with several vortices and shifted and distorted charged jets.

The additional contribution to the onset of instability can be made by the

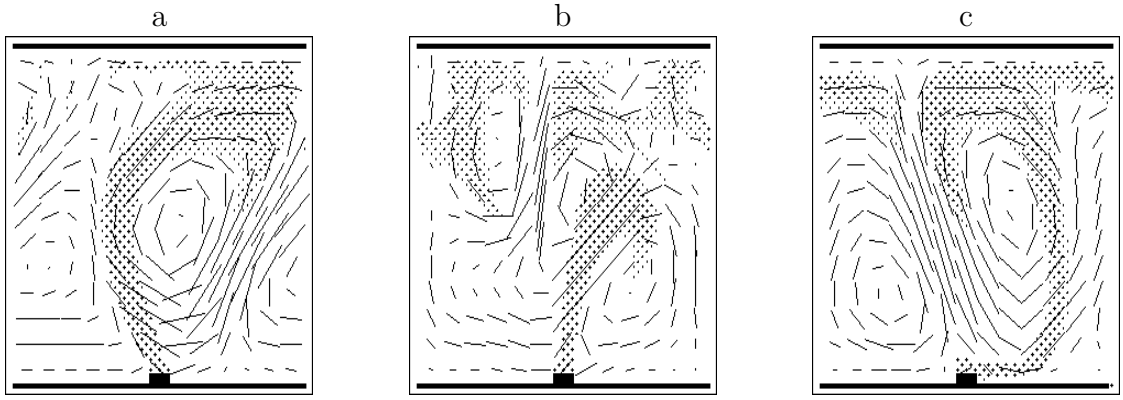

Figure 4.7. Development of EHD flow. Time is $t = 3{,}9 \cdot 10^4$ (a), $5 \cdot 10^4$ (b), $7{,}2 \cdot 10^4$ (c). Shown are the velocity field (lines) and the positive charge density (shades of gray)

strong electric field dependence of the injection current (conductivity of the layer adjacent to an electrode σ_0 is a rapidly increasing function of E). This effect was theoretically considered in [104], it was not taken into account in the present work.

4.4 Generation of vapor bubbles at the electrode surface in high electric field

One of the breakdown inception mechanisms is the bubble one. Bubbles can either pre-exist on the electrodes, or be generated in liquid after the voltage application. After the generation of bubbles, they grow and deform under the electric field action [105–108]. When bubbles achieve a certain size, the conditions for gas breakdown inside them appear. The breakdown of gas inside a bubble leads to a local enhancement of the electric field in a liquid. Under certain conditions, a further breakdown of dielectric liquid becomes possible [109]. For example, for the breakdown of water, the density should become lower than some critical one ($n < n_c$, at that electrons become quasi-free, for water $n_c = 10^{20}$ cm^{-3} [110]), and the bubble size should become sufficiently large for the critical electron avalanche to develop [111].

The generation of vapor bubbles at the initial stages of breakdown of liquids was observed experimentally in [102, 112–114]. Later, the growth of bubbles and the development of EHD-instability on their surface occur leading to the formation of streamer channels (see also chapter 5).

The thermal mechanism of bubble formation is connected with the local heat release in a liquid as a result of the heating by the electric current. When the temperature becomes higher than the boiling temperature of the liquid at a given pressure, the nuclei of vapor bubbles begin to appear which then expand

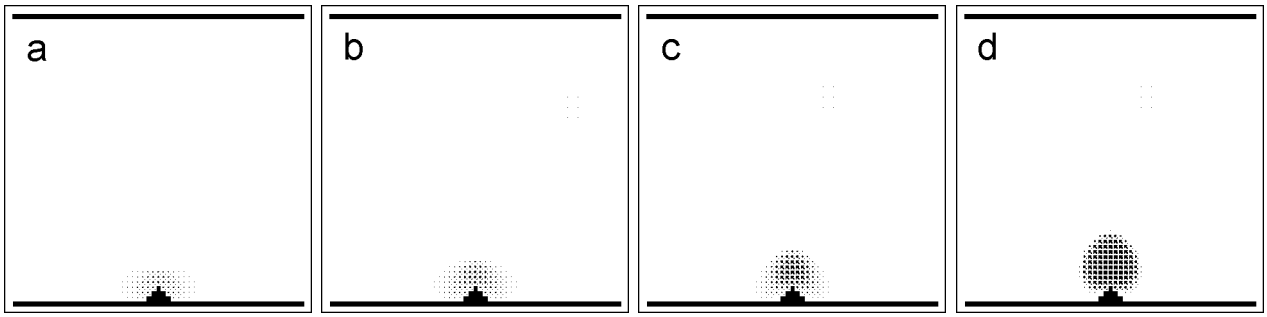

Figure 4.8. Generation and growth of cavitation vapor bubble in high electric field. Time is $t = 80$ (a), 100 (b), 120 (c), 140 (d)

due to the evaporation of new portions of liquid and due to the electric field action. A model was introduced in [111], in that bubble nuclei are formed in the regions of enhanced electric field on microtips by the local heating of liquid due to the field emission [115]. It was shown, that the inception time of the bubble nuclei makes the main contribution to the statistical lag time of a breakdown.

An alternative to the thermal mechanism is the homogenous nucleation of bubbles in the region of low (or negative) pressure even at the initial temperature. Such regions can exist near sharp tips and edges on the electrode surface, where electric field is high enough. This mechanism can be named electrodynamic cavitation. Possibility of bubble generation due to electrodynamic cavitation was mentioned in [8, 112, 116, 117].

When the charge injection from the electrode surface takes place in an electric field, liquid begins to move under the action of electrodynamic forces. At that, compression and rarefaction waves arise in liquid. Regions of low pressure adjacent to electrode appear, in which a phase transition at specified temperature can occur resulting in the generation of vapor micro-bubbles on the electrode surface (cavitation).

To simulate the process of bubble generation, the LBE model with interparticle interaction was used [3, 67] (see also chapter 1) which allows one to simulate phase transition, thus giving the possibility to model directly the process of electrodynamic cavitation. The interparticle interaction should be sufficiently strong $|G| > |G_c|$, and the initial density should be that of the dense phase. The permittivity of liquid ε was considered constant and independent on density (it is possible, if $\varepsilon \approx 1$, an example of such liquid is liquid helium with $\varepsilon = 1{,}05$). Hence, electrostriction forces were not taken into account.

Figure 4.8 presents different stages of the formation and growth of vapor bubble due to electrodynamic cavitation. The density inside the bubble decreased by three orders of magnitude. Thus, for the first time, generation and growth of vapor bubbles in high electric field near the electrode by the electro-

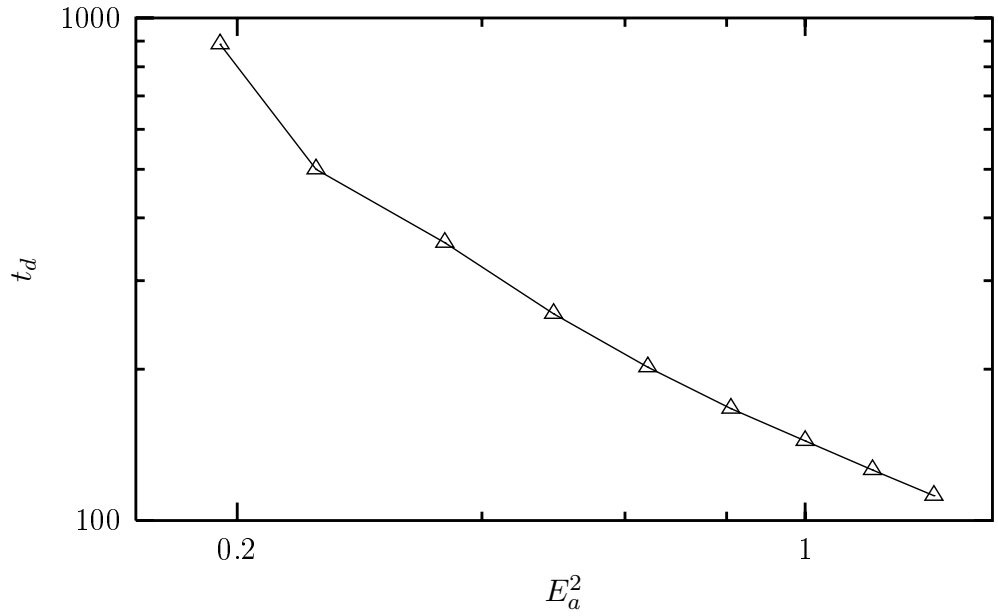

Figure 4.9. Electric field dependence of the bubble development time

dynamic cavitation mechanism was observed in simulations. The breakdown of gas inside bubbles can lead to further breakdown of liquid.

The generation and growth of bubbles at different applied voltages was investigated. Results are shown in fig. 4.9. The time between the voltage application and the generation of a bubble of certain size ($R \approx 5$ lattice units) depended strongly on the electric field strength. This time increased sharply when the electric field decreased. If the field was lower than a certain critical value (in our case $E_{cr} \approx 0{,}44$), the bubble did not appear. Thus, the cavitation mechanism of bubble generation is of the threshold nature.

At higher fields, the development time is approximately inversely proportional to the square of the average electric field E_a ($t_d \sim E_a^{-2}$, fig. 4.9). The same dependence of the development time on the energy release $w = j \cdot E$ was mentioned in [111] for the breakdown of liquid argon and water ($t_d \sim w^{-1}$). In our case, j is proportional to E_a, hence, the energy release is proportional to E_a^2.

The results obtained agree with the conclusions of [102], where the expression for the bubble size vs. time was obtained $R(t) \sim \left(E^2 t\right)^{2/3}$ for the case of viscosity-dominated bubble growth. For fixed R it also leads to $t_d \sim E^{-2}$.

Summary

A lattice Boltzmann equation model for simulation of electrohydrodynamic flows is proposed. Three methods for computation of the convective charge

transport were realized (the method of "LBE-particles", the method of mean velocity, and the method of additional LBE component). Formulas for numeric diffusivity were derived for all methods.

The simulation was carried out of two-dimensional electrohydrodynamic flows caused by the charge injection from a protrusion on the electrode. Under these conditions, a flow of liquid in the shape of a plane vortical dipole is formed. At the initial stage, the flow has strong pulsations caused by the electric field decrease upon the protrusion after the injection of next charge lump. At later stages, the instability of the main flow mode is more significant. The flow symmetry breaks, jets shift and distort, and additional vortices appear.

For the first time, the possibility of micro-bubble generation in high electric field on the electrode surface by the electrodynamic mechanism was confirmed by direct simulations. The electric breakdown of gas in bubbles generated can result then in the breakdown of liquid. The time of bubble development was shown to increase with the decrease in electric field, this effect is of the threshold character. The voltage dependence of the bubble development time was obtained which agrees with theoretical predictions and experimental results.

The method developed is sufficiently simple and effective. It is promising for the simulation of electrohydrodynamic problems.

Chapter 5

Structure and dynamics of "plasma" channels at the electric breakdown of dielectric liquids

The electric breakdown occurs when the electric field in dielectric liquid becomes sufficiently high. In chapter 4, the consequence of processes accompanying this phenomenon was described along with one possible mechanism of the generation of breakdown nuclei, the development of cavitation bubbles on the electrode surface. Further breakdown of gas inside bubbles when they reache the critical size results in generation of conductive regions. Such conductive regions can be generated also by other mechanisms. The fast growth of thin plasma channels (streamers) proceeds later from these regions. When a streamer reaches the opposite electrode, a conductive channel is formed.

In this chapter, the propagation of single streamer tip and the expansion dynamics of the discharge channel in liquid are considered taking into account the flux of fluid into channel plasma.

5.1 Streamer propagation in dielectric liquid

The flow of dielectric liquid was simulated by the LBE method. Computations were carried out on a square lattice with 4 values of particle velocity 0, 1, $\sqrt{2}$, and 2 (13 possible velocity vectors) [3, 32], fig. 1.4,*b*. This model allows one to introduce liquid temperature and to simulate energy release. If at a node the average kinetic energy per one particle ε ("temperature") exceeded the critical value ε_*, this node became conductive, and an energy release began at it. The energy release continued until $\varepsilon \leq \varepsilon_{max}$. Under such conditions, heat released in sufficiently thin layer near the channel boundary that corresponds to the real case. Indeed, conductive and radiative heat transport inside the channel is sufficiently fast, therefore, all the energy released is transferred from inner

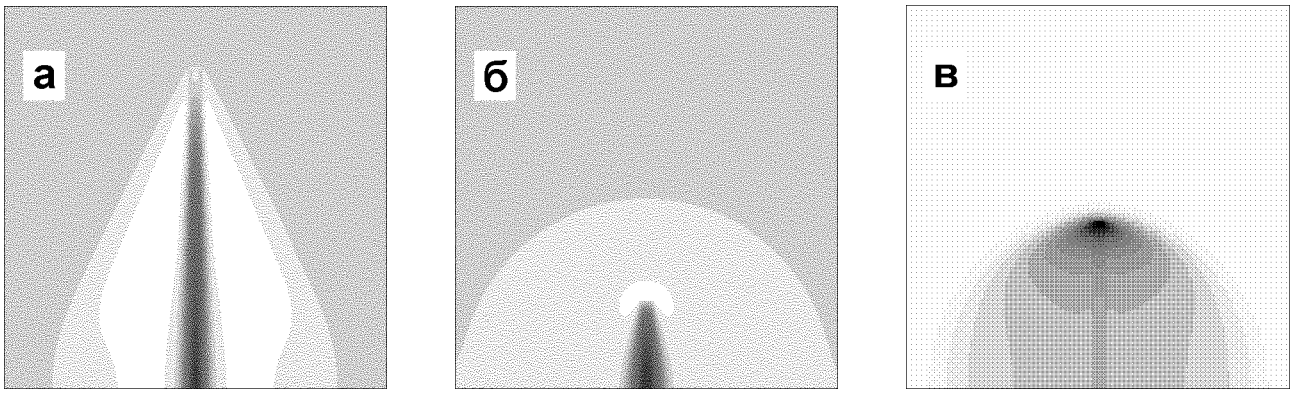

Figure 5.1. Density distribution. a — $v/c = 2{,}5$, $t = 100$; b — $v/c = 0{,}5$, $t = 140$ (darker color means lower density); c — pressure field, $v/c = 1{,}0$, $t = 130$ (darker color corresponds to higher pressure)

regions to the boundaries and it is absorbed in a thin layer of liquid. The inner structure of a channel boundary is considered more detailed in the following section.

Computations were carried out of the single streamer tip propagation at the breakdown of dielectric liquid (fig. 5.1). Expansion of the conductive channel and formation of compression waves were observed. These waves propagated with the sound velocity in a dielectric liquid (in this case, $c = 1$). When the velocity of the streamer tip was greater than c, a divergent shock wave having a nearly conical front was formed (fig. 5.1,*a*). Such waves were observed experimentally at pre-breakdown stages of streamer propagation in many works, e.g., in experiments [118]. When the the velocity of streamer tip was subsonic, the compression wave had spherical front (fig. 5.1,*b,c*).

5.2 Channel stage of the electric discharge in liquid

After the closing of the interelectrode gap by one of the initial streamers, the channel stage of the electric discharge begins.

For the one-dimensional problem of expansion of a conductive channel, a self-similar solution exists when the following three requirements are satisfied:
1. The power released in the channel $W = const$.
2. The heat conductivity inside the channel is high, and one can roughly consider that the energy released is completely transferred to the channel boundary by both the conductive heat flux and radiation.
3. The total heat flux from the channel is completely absorbed in a thin layer of liquid, leading to transition of the liquid to the plasma of the channel after dissociation and partial ionization of the fluid. The absorption of radiation in

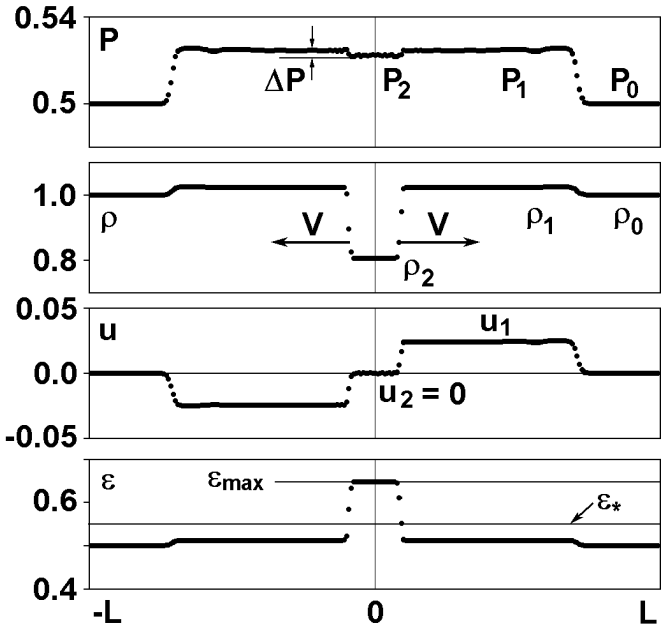

Figure 5.2. Structure of self-similar flow. Computations by the LBE method. P is the pressure, ρ is the density, u is the mass velocity, ε is the average kinetic energy per one particle ("temperature")

liquids increases sharply at the photon energy of order of 10 eV. Experimental data on the absorption spectrum of water in the far ultraviolet region [119] indicate that radiation with a wavelength $\lambda < 1600$ Å is almost entirely absorbed in a thin layer of liquid $\sim 10^{-4}$ cm.

Under these requirements, the mass velocity of "plasma" inside the conductive channel is zero, and the temperature, density and pressure are constant both over the channel cross-section and in time.

Figure 5.2 presents the flow structure for this self-similar solution obtained in simulation by the LBE method.

Transition of liquid to a conductive phase takes place in a transition layer liquid — "plasma". This transition proceeds through the flux of molecules of liquid to the channel plasma after their dissociation and partial ionization. At the channel stage of electric discharge, the molecular flux into the channel can be considerably greater than $j \sim 2 \cdot 10^{24}\ ^{-1}.^{-2}$ [120]. At the initial stage of streamer propagation, the temperature in conductive channel is comparatively low ($\sim$ 3000 K) [121], therefore, the density of substance in it differs slightly from the liquid density. Thus, the boundary between the conductive channel and the surrounding liquid is not an impenetrable piston. If the thickness of the transition layer is small comparing with the channel radius, the transition layer can be considered as a quasi-stationary gas-dynamic discontinuity. In the reference frame of the transition layer, the mass and momentum conservation laws are given by

$$\begin{aligned} &\rho_1 D = \rho_2 \upsilon_2, \\ &p_1 + \rho_1 D^2 = p_2 + \rho_1 D \upsilon_2. \end{aligned} \tag{5.1}$$

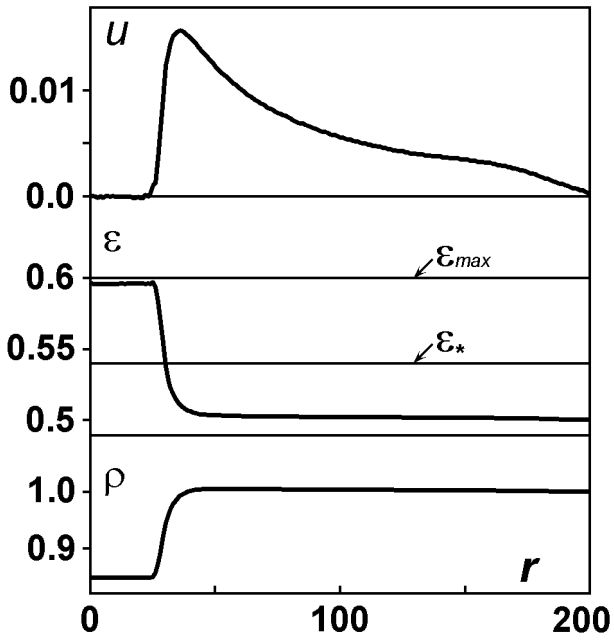

Figure 5.3. Self-similar liquid flow at the expansion of cylindrical streamer channel. Time is $t = 180$. ρ is the density, u is the mass velocity, ε is the average kinetic energy per unit mass ("temperature")

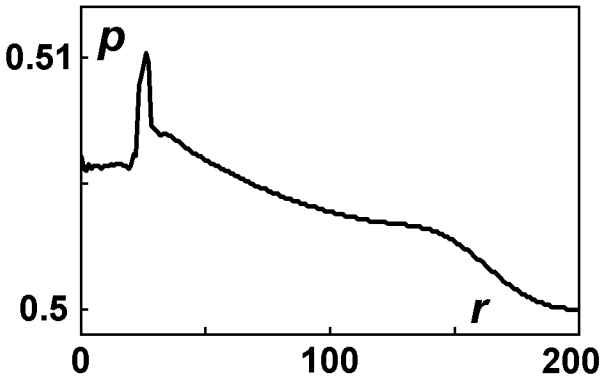

Figure 5.4. Pressure graph at the expansion of cylindrical channel. Time is $t = 160$

Here p is the pressure, ρ is the density, u is the mass velocity of liquid, D is the velocity of inflowing liquid, $v_2 = V - u_2$ is the plasma velocity relative to the discontinuity, $V = u_1 + D$ is the observable velocity of channel expansion (see fig. 5.2).

It follows from (5.1), that a small pressure jump $p_1 = p_2 + \rho_2 v_2(v_2 - D)$ arises at the discontinuity (inside the channel the pressure is lower). This effect is caused by the mass inflow through the channel boundary. In the self-similar case, the mass velocity inside the channel is $u_2 = 0$, hence, $v_2 = V$, and the pressure difference is $\Delta p = p_1 - p_2 = \rho_2 V u_1$ that exactly coincides with the value obtained in the LBE computations (fig. 5.2).

The self-similar solution for the one-dimensional problem of the expansion of a cylindrical channel was also obtained (figs. 5.3 and 5.4). The only difference in conditions of its existence from those for the planar case is that the rate of energy release increases with time as $W = \alpha t$ [122].

Self-similar regimes of the expansion of a cylindrical streamer channel were

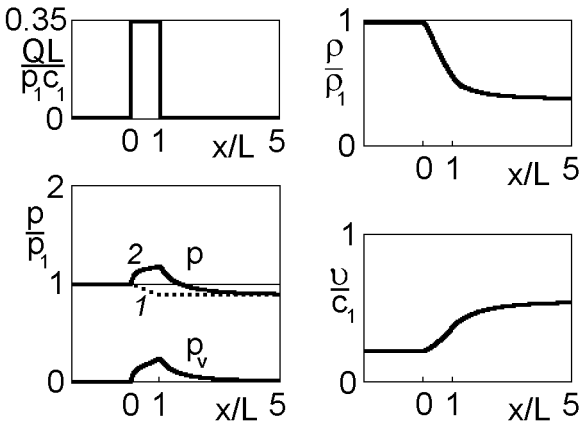

Figure 5.5. Structure of viscous transition layer for constant energy release

investigated for $W = \alpha t$ under conditions of energy release in a thin layer $\varepsilon_* < \varepsilon < \varepsilon_{max}$. Figure 5.3 presents the computation results. The mass velocity inside the channel was $u \approx 0$, and outside it approximately $u \sim 1/r$ up to the front of the divergent shock wave. The strength of this wave depended on the energy release and in the present case it was small. There were disturbances in the conductive channel, most noticeable on the velocity plots.

5.3 Model of the transition layer

Figure 5.4 presents the pressure graph corresponding to the computation of fig. 5.3. Besides the pressure difference Δp (5.1), there is a small pressure peak localized inside the transition layer. In order to explain this phenomenon, the one-dimensional model of viscous transition layer was considered.

Let the energy release takes place in a layer of thickness L. In the comoving reference frame, liquid flows into the zone of energy release with the velocity D. The conservation laws for mass, momentum and energy are given in the case of zero heat conductivity by:

$$\begin{aligned} &\rho v = \rho_1 D, \\ &p + \rho v^2 - (\frac{4}{3}\eta + \zeta)\frac{dv}{dx} = p_1 + \rho_1 D^2, \\ &\frac{\gamma}{\gamma - 1} pv + \rho v \frac{v^2}{2} - (\frac{4}{3}\eta + \zeta) v \frac{dv}{dx} = \frac{\gamma}{\gamma - 1} p_1 D + \rho_1 \frac{D^3}{2} + v \int_0^x \frac{Q}{v} dx. \end{aligned} \tag{5.2}$$

Here v is the current liquid velocity, γ is the adiabata index of the gas in transition layer, Q is the rate of energy release, η is the dynamic viscosity, ζ is the second viscosity.

The system (5.2) was solved numerically. Computation results are shown in fig. 5.5 for $p_1 = 1$, $c_1 = 1$, $D/c_1 = 0.2$, $\gamma = 5/3$ in the case of constant

energy release in a layer of thickness $L = 1$ (dimensionless energy release was $QL/p_1c_1 = 0.35$, dimensionless viscosity was $(4/3\eta+\zeta)c_1/(p_1L) = 1$). Without viscosity, the pressure decreases monotonically in the zone of energy release (fig. 5.5, curve 1). The pressure peak can arise in the transition layer due to viscous part of the stress tensor $p_V = (4/3\eta + \zeta)dv/dx$ (fig. 5.5, curve 2). It follows from second equation of (5.2): the pressure is $p = p_1+\rho_1 D(D-v)+p_V$. One can estimate the value of this peak for constant viscosity, assuming $dv/dx \approx V/L$. One obtains $p_V \sim 10^5$ Pa $\sim 1\%$ of p_1 for typical parameters of streamer channel expansion at the breakdown of liquids $V \sim 100$ m/s [118], $\eta = 10^{-3}$ kg/m·s $L \sim 10^{-6}$ m [120]. The pressure p_1 in liquid near the cylindrical discharge channel was estimated by its expansion velocity V [123]. For $V \sim 100$ m/s in water, one obtains $p_1 \approx 3 \cdot 10^7$ Pa. The relative value of the pressure peak in the transition layer for the LBE method is of the same order (fig. 5.4).

Summary

Use of the LBE method allows one to model qualitatively the flow of dielectric liquid at the streamer tip propagation and the flow at the channel stage of the electric discharge. In the case of the supersonic streamer velocity, divergent shock waves with conical front are observed. At the boundary of the discharge channel, the pressure jump is observed caused by the reactive force due to flow of fluid into the channel. The computed value of this pressure jump is equal to the theoretical one.

The channel boundary is a thin transition layer where the energy release occurs which forces the transition of liquid to the channel plasma. Inside the transition layer, the pressure changes non-monotonically due to viscous part of the stress tensor. Computed value of the pressure peak agrees with the theoretic estimates.

CONCLUSIONS

The main results obtained are:

1. Simulation of convective detonation waves in a porous medium was carried out.

   A new model was proposed based on the lattice gas method. This model allows one to take into account the stochastic nature of this phenomenon. Propagation of the wave front and its curved shape were obtained automatically in computations in contrast with existing continual models. Computed wave velocity and pressure profile were in good agreement with experimental ones.

2. Based on the numerical investigation of the component mixing process, a possible mechanism was explained of the time and grain size dependence of electric conductivity in detonation products of heterogeneous HEs.

   Flow development for different initial geometry was considered. Time dependencies of detonation product conductivity of heterogeneous HEs were obtained. The dependencies obtained are in qualitative agreement with the experimental results.

3. The modification of the LBE method was developed for simulation of electrohydrodynamic flows. Several methods to compute the convective charge transport were considered. Theoretical values of the numerical diffusivity were compared with the computation results.

   Development of EHD-flow in different geometry was studied. In two-dimensional case, the flow has oscillatory character caused by the charge injection in discrete lumps that reduce the electric field. As the voltage between electrodes is increased, the instability of liquid flow emerges which breaks the flow symmetry.

4. For the first time, the possibility of micro-bubble generation in high electric field on the electrode surface by the electrodynamic mechanism was confirmed by direct simulations. At certain conditions, the emergence of a region of gas phase was observed in computations. Such a bubble was

generated in the region of high electric field (near the tip) due to to electrodynamic cavitation. The electric breakdown of gas in bubbles generated can further result in the breakdown of liquid.

5. The model was developed which describes the streamer tip propagation and the dynamics of the electric discharge channel expansion in liquid with generation of shock waves. The planar and the cylindrical cases were considered.

   The divergent shock waves were observed at the streamer tip propagation with supersonic velocity and at the channel expansion due to energy release inside it.

6. The inner structure of the channel boundary (the transition layer "liquid–plasma") was computed taking into account the liquid viscosity. The non-monotonic pressure variation across the boundary due to viscous tension is shown. Theoretical estimates of the pressure step on the channel boundary and of the pressure peak inside the transition layer agree well with computation results.

Main results were presented on scientific conferences, among them:

- International Symposium on Electrical Insulation (Arlington, 1998)
- 13^{th} and 14^{th} International Conferences on Dielectric Liquids (Nara, 1999, Graz, 2002)
- 2^{nd} International Workshop on Electric Conduction, Convection and Breakdown of Liquids (Grenoble, 2000)
- 12^{th} Symposium on Combustion and Explosion (Chernogolovka, 2000)
- V and VI International Conferences "Modern Problems of Electrophysics and Electrohydrodynamics of Liquids" (Sankt-Petersburg, 1998, 2000)
- II, III, IV and V Siberian Workshops "Mathematical Problems of Fluid Mechanics" (Novosibirsk, 1998, 1999, 2000, 2001)
- International Conference "III Khariton's Topic Scientific Readings" (Sarov, 2001)
- International Conference "VI Zababakhin's Scientific Readings" (Sneginsk, 2001)
- III and IV International Workshops "Pulse Processes in Fluid Mechanics" (Nikolaev, 1999, 2001)

The results obtained are published in [1–14].

Bibliography

[1] A.L. Kupershtokh and D.A. Medvedev. Simulation of Gas-dynamic Flows during Streamer Propagation at Liquid Dielectrics Breakdown. In *Conference record of the 1998 IEEE Int. Symposium on Electrical Insulation*, pages 611–614, Arlington, VA, 1998.

[2] A.L. Kupershtokh and D.A. Medvedev. Modeling of gas-dynamic flows during streamer propagation at the breakdown of dielectric liquids. In *Modern problems of electrophysics and electrohydrodynamics of liquids (in russian). Proc. of V Int. Conference*, pages 126–130, Sankt-Petersburg, Russia, 1998.

[3] D.A. Medvedev and A.L. Kupershtokh. Lattice Boltzmann equation method for gas dynamics problems. In *Dinamika Sploshnoi Sredy (Dynamics of Continuous Medium)*, pages 117–121. N 114. Novosibirsk, Inst. of Hydrodynamics, 1999.

[4] D.A. Medvedev. Lattice Boltzmann equation method in problems of fluid dynamics. In *Proc. of III Workshop "Pulse processes in fluid mechanics, Nikolaev, Ukraine"*, pages 23–24. IIPT NAS Ukraine (in russian), 1999.

[5] A.P. Ershov, A.L. Kupershtokh, and D.A. Medvedev. Simulation of combustion waves in a porous medium by the cellular automata method. In *Dinamika Sploshnoi Sredy (Dynamics of Continuous Medium)*, pages 117–121. N 115. Novosibirsk, Inst. of Hydrodynamics, 1999.

[6] A.L. Kupershtokh and D.A. Medvedev. Simulation of Hydrodynamic Flows during Streamer Propagation in Dielectric Liquids. In *Proc. of 1999 IEEE 13th Int. Conference on Dielectric Liquids*, pages 179–182, Nara, Japan, 1999. IEEE N 99CH36213.

[7] A.L. Kupershtokh and D.A. Medvedev. Structure and dynamics of "plasma" channels at the breakdown of dielectric liquids. In *Dinamika Sploshnoi Sredy (Dynamics of Continuous Medium)*, pages 137–141. N 116. Novosibirsk, Inst. of Hydrodynamics, 2000.

[8] D.A. Medvedev and A.L. Kupershtokh. Use of the Lattice Boltzmann Equation Method to Simulate Charge Transfer and Electrohydrodynamic Phenomena in Dielectric Liquids. In P. Atten and A. Denat, editors, *Electrical Conduction, Convection and Breakdown in Fluids. Proc. 2^{nd} Int. Workshop*, pages 60–63, Grenoble, France, 2000.

[9] A.P. Ershov, D.A. Medvedev, N.P. Satonkina, O.A. Dibirov, S.V. Tsykin, and Yu.V. Yanilikn. Mesoprocesses at detonation of TNT/RDX mixtures. In *Chemical physics of combustion and explosion processes. 12^{th} Symposium on combustion and explosives. Part II*, pages 129–131. Chernogolovka: IPCP RAS, 2000 (in russian), 2000.

[10] A.P. Ershov, A.L. Kupershtokh, and D.A. Medvedev. Simulation of Convective Detonation Waves in a Porous Medium by the Lattice Gas Method. *Combustion, Explosion and Shock Waves*, 37(2):206–213, 2001. (Russian edition: Fizika Goreniya i Vzrywa, pp. 94–102).

[11] D.A. Medvedev, A.P. Ershov, and Yu.V. Yanilkin. Simulation of mixing in two-component system. In *Proc. of Int. Conference "III Khariton's scientific readings"*, pages 247–253. Sarov, RFNC-VNIIEF, 2002, 2001. (in russian).

[12] A.L. Kupershtokh and D.A. Medvedev. Lattice Boltzmann equation method for electrohydrodynamics. In *Dinamika Sploshnoi Sredy (Dynamics of Continuous Medium)*, pages 117–121. N 118. Novosibirsk, Inst. of Hydrodynamics, 2001.

[13] D.A. Medvedev and A.P. Ershov. Simulation of mixing of heterogeneous HE components behind the detonation front. In *Dinamika Sploshnoi Sredy (Dynamics of Continuous Medium)*, pages 126–129. Issue 118. Novosibirsk, Inst. of Hydrodynamics, 2001.

[14] D.A. Medvedev and A.L. Kupershtokh. Modeling of Electrohydrodynamic Flows and Micro-bubbles Generation in Dielectric Liquid by Lattice Boltzmann Equation Method. In *Proc. of 2002 IEEE 14^{th} Int. Conference on Dielectric Liquids*, pages 45–48, Graz, Austria, 2002. IEEE N 02CH37319.

[15] J. Hardy, O. de Pazzis, and Y. Pomeau. Molecular dynamics of a classical lattice gas: transport properties and time correlation functions. *Physical Review A*, 13(5):1949–1961, 1976.

[16] U. Frisch, B. Hasslacher, and Y. Pomeau. Lattice-gas automata for the Navier-Stokes equation. *Physical Review Letters*, 56(14):1505–1508, 1986.

[17] G. McNamara and G. Zanetti. Use of the Boltzmann equation to simulate lattice-gas automata. *Physical Review Letters*, 61(20):2332–2335, 1988.

[18] F.J. Higuera and J. Jiménez. Boltzmann approach to lattice gas simulation. *Europhysics Letters*, 9(7):663–668, 1989.

[19] A.P. Ershov. Gas dynamics of cellular automata (review). *Fizika Gorenia i Vzrywa (Combustion, Explosion and Shock Waves)*, 30(1):107–116, 1994. (Russian edition: pp. 107–117).

[20] S. Chen, M. Lee, K.H. Zhao, and G.D. Doolen. A lattice gas model with temperature. *Physica D*, 37:42–59, 1989.

[21] D. d'Humières, P. Lallemand, and U. Frisch. Lattice gas model for 3D hydrodynamics. *Europhysics Letters*, 2(4):291–297, 1986.

[22] D.H. Rothman and J.M. Keller. Immiscible Cellular-Automaton Fluids. *Journal of Statistical Physics*, 52(3/4):1119–1127, 1988.

[23] C. Appert and S. Zaleski. Lattice gas with a liquid-gas transition. *Physical Review Letters*, 64(1):1–4, 1990.

[24] D.H. Rothman and S. Zaleski. Lattice-gas models of phase separation: interfaces, phase transitions, and multiphase flow. *Reviews of Modern Physics*, 66(4):1417–1479, 1994.

[25] X. He and L.-S. Luo. A priori derivation of the lattice Boltzmann equation. *Physical Review E*, 55(6):6333–6336, 1997.

[26] T. Abe. Derivation of the lattice Boltzmann method by means of the discrete ordinate method for the Boltzmann equation. *Journal of Computational Physics*, 131(1):241–246, 1997.

[27] X. He, X. Shan, and G. Doolen. Discrete Boltzmann equation model for nonideal gases. *Physical Review E*, 57(1):R13–R16, 1998.

[28] L.-S. Luo. Unified theory of lattice Boltzmann models for nonideal gases. *Physical Review Letters*, 81(8):1618–1621, 1998.

[29] L.-S. Luo. Theory of the lattice Boltzmann method: Lattice Boltzmann models for nonideal gases. *Physical Review E*, 62(4):4982–4996, 2000.

[30] P. Bhatnagar, E.P. Gross, and M.K. Krook. A model for collision processes in gases. I. Small amplitude processes in charged and neutral one-component systems. *Physical Review*, 94(3):511–525, 1954.

[31] Y.H. Qian, D. d'Humières, and P. Lallemand. Lattice BGK models for Navier-Stokes equation. *Europhysics Letters*, 17(6):479–484, 1992.

[32] Y.H. Qian. Simulating thermohydrodynamics with lattice BGK models. *Journal of Scientific Computing*, 8(3):231–242, 1993.

[33] S. Chapman and T.G. Cowling. *The Mathematical Theory of Nonuniform Gases*. Cambridge University Press, 1970.

[34] Y.H. Qian and S.A. Orszag. Lattice BGK models for the Navier-Stokes equation: nonlinear deviation in compressible regimes. *Europhysics Letters*, 21(3):255–259, 1993.

[35] P.J. Dellar. Bulk and shear viscosities in lattice Boltzmann equation. *Physical Review E*, 64:031203–1–031203–11, 2001.

[36] S. Chen and G. Doolen. Lattice Boltzmann method for fluid flows. *Annual Review of Fluid Mechanics*, 30:329–364, 1998.

[37] Y.H. Qian. Fractional propagation and the elimination of staggered invariants in lattice-BGK models. *International Journal of Modern Physics C*, 8(4):753–762, 1997.

[38] R. Zhang, H. Chen, Y.H. Qian, and S. Chen. Effective volumetric lattice Boltzmann scheme. *Physical Review E*, 63:056705–1–056705–6, 2001.

[39] S. Hou, Q. Zou, S. Chen, G. Doolen, and A.C. Cogley. Simulation of cavity flow by the lattice Boltzmann method. *Journal of Computational Physics*, 118(2):329–347, 1995.

[40] X. He and G. Doolen. Lattice Bolzmann method on curvilinear coordinates system: Flow around a circular cylinder. *Journal of Computational Physics*, 134(2):306–315, 1997.

[41] D.O. Martinez, W.H. Matthaeus, S. Chen, and D.C. Montgomery. Comparison of spectral method and lattice Boltzmann simulations of two-dimensional hydrodynamics. *Physics of Fluids*, 6(3):1285–1298, 1994.

[42] X. He, L.-S. Luo, and M. Dembo. Some progress in lattice Boltzmann method. Part I. Nonuniform mesh grids. *Journal of Computational Physics*, 129(2):357–363, 1996.

[43] F. Nannelli and S. Succi. The lattice Boltzmann equation on irregular lattices. *Journal of Statistical Physics*, 68(3/4):401–407, 1992.

[44] G. Amati, S. Succi, and R. Benzi. Turbulent channel flow simulations using a coarse-grained extension of the lattice Boltzmann method. *Fluid Dynamics Research*, 19:289–302, 1997.

[45] O. Filippova and D. Hänel. Grid refinement for lattice-BGK models. *Journal of Computational Physics*, 147:219–228, 1998.

[46] O. Filippova and D. Hänel. Acceleration of lattice-BGK schemes with grid refinement. *Journal of Computational Physics*, 165:407–427, 2000.

[47] C.-L. Lin and Y.G. Lai. Lattice Boltzmann method on composite grids. *Physical Review E*, 62(2):2219–2225, 2000.

[48] S. Chen, H. Chen, D. Martinez, and W. Matthaeus. Lattice Boltzmann model for simulation of magnetohydrodynamics. *Physical Review Letters*, 67(27):3776–3779, 1991.

[49] S. Succi, M. Vergasola, and R. Benzi. Lattice Boltzmann scheme for two-dimensional magnetohydrodynamics. *Physical Review A*, 43(8):4521–4524, 1991.

[50] Y.H. Qian and Y.F. Deng. A lattice BGK model for viscoelastic media. *Physical Review Letters*, 79(14):2742–2745, 1997.

[51] O. Dardis and J. McCloskey. Lattice Boltzmann scheme with real numbered solid density for the simulation of flow in porous media. *Physical Review E*, 57(4):4834–4837, 1998.

[52] F.J. Alexander, S. Chen, and J.D. Sterling. Lattice Boltzmann thermohydrodynamics. *Physical Review E*, 47(4):R2249–R2252, 1993.

[53] Y. Chen, H. Ohashi, and M. Akiyama. Thermal lattice Bhatnagar-Gross-Krook model without nonlinear deviations in macrodynamical equations. *Physical Review E*, 50(4):2776–2783, 1994.

[54] Y. Chen, H. Ohashi, and M. Akiyama. Heat transfer in lattice BGK modelled fluids. *Journal of Statistical Physics*, 81(1/2):71–85, 1995.

[55] M. Soe, G. Vahala, P. Pavlo, L. Vahala, and H. Chen. Thermal lattice Boltzmann simulations of variable Prandtl number turbulent flows. *Physicl Review E*, 57(4):4227–4237, 1998.

[56] P. Pavlo, G. Vahala, and L. Vahala. Higher order isotropic velocity grids in lattice methods. *Physical Review Letters*, 80(18):3960–3963, 1998.

[57] N. Cao, S. Chen, S. Jin, and D. Martinez. Physical symmetry and lattice symmetry in the lattice Boltzmann method. *Physical Review E*, 55(1):R21–R24, 1997.

[58] A. Renda, G. Bella, S. Succi, and I.V. Karlin. Thermohydrodynamic lattice BGK schemes with non-perturbative equilibria. *Europhysics Letters*, 41(3):279–283, 1998.

[59] X. Shan. Simulation of Rayleigh–Bénard convection using a lattice Boltzmann method. *Physical Review E*, 55(3):2780–2788, 1997.

[60] X. He, S. Chen, and G.D. Doolen. A novel thermal model for the lattice Boltzmann method in incompressible limit. *Journal of Computational Physics*, 146(2):282–300, 1998.

[61] B.J. Palmer and D.R. Rector. Lattice Boltzmann algorithm for simulating thermal flow in compressible fluids. *Journal of Computational Physics*, 161(1):1–20, 2000.

[62] G.R. McNamara, A.L. Garcia, and B.J. Alder. Stabilization of Thermal Lattice Boltzmann Models. *Journal of Statistical Physics*, 81(1/2):395–408, 1995.

[63] F.L. Hinton, M.N. Rosenbluth, S.K. Wong, Y.R. Lin-Liu, and R.L. Miller. Modified lattice Boltzmann method for compressible fluid simulations. *Physical Review E*, 63:061212–1–061212–9, 2001.

[64] A.K. Gunstensen, D.H. Rothman, S. Zaleski, and G. Zanetti. Lattice Boltzmann model of immiscible fluids. *Physical Review A*, 43(8):4320–4327, 1991.

[65] D. Grunau, S. Chen, and K. Eggert. A lattice Boltzmann model for multiphase fluid flows. *Physics of Fluids A*, 5(10):2557–2562, 1993.

[66] R. Holme and D.H. Rothman. Lattice-gas and lattice-Boltzmann models of miscible fluids. *Journal of Statistical Physics*, 68(3/4):409–429, 1992.

[67] X. Shan and H. Chen. Lattice Boltzmann model for simulating flows with multiple phases and components. *Physical Review E*, 47(3):1815–1819, 1993.

[68] X. Shan and H. Chen. Simulation of nonideal gases and liquid-gas transitions by the lattice Boltzmann equation. *Physical Review E*, 49(4):2941–2948, 1994.

[69] X. Shan and G. Doolen. Multicomponent lattice-Boltzmann model with interparticle interaction. *Journal of Statistical Physics*, 81(1/2):379–393, 1995.

[70] X. Shan and G. Doolen. Diffusion in a multicomponent lattice Boltzmann equation model. *Physical Review E*, 54(4):3614–3620, 1996.

[71] S. Ponce Dawson, S. Chen, and G.D. Doolen. Lattice Boltzmann computations for reaction-diffusion equations. *Journal of Chemical Physics*, 98(2):1514–1523, 1993.

[72] X. He, R. Zhang, S. Chen, and G.D. Doolen. On the three-dimensional Rayleigh-Taylor instability. *Physics of Fluids*, 11(5):1143–1152, 1999.

[73] G.M. Mamontov, V.V. Mitrofanov, and V.A. Subbotin. Detonation regimes of the gaseous mixture in inert porous medium. In *Detonation. Proc. VI All-Union Symp. on Combustion and Explosion*, pages 106–110, Chernogolovka, 1980. (in Russian).

[74] G.A. Lyamin. Heterogeneous detonation in a rigid porous medium. *Fizika Gorenia i Vzrywa (Combustion, Explosion and Shock Waves)*, 20(6):134–138, 1984.

[75] G.A. Lyamin and A.V. Pinaev. Fuel properties effect on the heterogeneous detonation parameters in a porous medium. In *Dinamica Sploshnoi Sredy (Dynamics of Continuous Medium)*, pages 95–101. N 88. Novosibirsk, Inst. of Hydrodynamics, 1988.

[76] A.V. Pinaev and G.A. Lyamin. To the structure of gas-film and gaseous detonation in an inert porous medium. *Fizika Gorenia i Vzrywa (Combustion, Explosion and Shock Waves)*, 28(5):97–102, 1992.

[77] G.A. Lyamin and A.V. Pinaev. Heterogeneous detonation (gas-film) in porous medium. The region of existence and limits. *Fizika Gorenia i Vzrywa (Combustion, Explosion and Shock Waves)*, 28(5):102–108, 1992.

[78] A.V. Pinaev and G.A. Lyamin. Low-velocity detonation of high explosive in evacuated porous medium. *Doclady RAN*, 325(3):498–501, 1992.

[79] V.V. Andreev and L.A. Lukyanchikov. To the propagation mechanizm of low-velocity detonation in powdered PETN after spark initiation. *Fizika Gorenia i Vzrywa (Combustion, Explosion and Shock Waves)*, 10(6):912–919, 1974.

[80] V.V. Andreev, A.P. Ershov, and L.A. Lukyanchikov. Two-phase low-velocity detonation of a porous explosive. *Fizika Gorenia i Vzrywa (Combustion, Explosion and Shock Waves)*, 20(3):89–93, 1984.

[81] A.P. Ershov. Isothermal detonation and its stochastic modeling. *Fizika Gorenia i Vzrywa (Combustion, Explosion and Shock Waves)*, 30(3):366–376, 1994. (Russian edition: pp. 112–124).

[82] A.P. Ershov, A.L. Kupershtokh, and A.Ya. Dammer. Structured flows in porous media modeling by stochastic methods. In C.T. et al Crowe, editor, *Numerical Methods for Multiphase Flows. Proc. Int. Symp. on Multiphase Flows*, pages 59–64, Lake Tahoe, NV, 1994. N.Y.: ASME, FED-Vol. 185,.

[83] S. Ergun. Fluid flow through packed columns. *Chem. Eng. Progr.*, 48(2):89–94, 1952.

[84] D.P. Jones and H. Krier. Gas flow resistance measurements through packed beds at high Reynolds numbers. *Trans. ASME. Journal of Fluid Engineering*, 105:168–173, 1983.

[85] W.H. Denton. The heat transfer and flow resistance for fluid flow through randomly packed spheres. In *General Discussion on Heat Transfer.*, pages 370–373. London. Institute of Mechanical Engineering and ASME, 1951.

[86] A.P. Ershov. A convective detonation wave in a porous structure. *Fizika Gorenia i Vzrywa (Combustion, Explosion and Shock Waves)*, 33(1):81–88, 1997. (Russian edition: pp. 98–106).

[87] J.-F. Haas and B Sturtevant. Interaction of weak shock waves with cylindrical and spherical gas inhomogeneities. *Journal of Fluid Mechanics*, 181(1):41–76, 1987.

[88] N. Cowperthwaite. The interaction of a plane shock and a dense spherical inhomogeneity. *Physica D*, 37(1-3):264–269, 1989.

[89] J.W. Jacobs. The dynamics of shock accelerated light and heavy gas cylinders. *Physics of Fluids*, 5(9):2239–2247, 1993.

[90] M.A. Jones and J.W. Jacobs. A membraneless experiment for the study of Richtmyer–Meshkov instability of a shock-accelerated gas interface. *Physics of Fluids*, 9(10):3078–3085, 1997.

[91] O. Sadot, U. Alon, D. Oron, L. A. Levin, G. Erez, G. Ben-Dor, and D. Shvarts. Study of nonlinear evolution of single-mode and two-bubble

interaction under Richtmyer–Meshkov instability. *Physical Review Letters*, 80(8):1654–1657, 1998.

[92] P.M. Rightley, P. Vorobieff, R. Martin, and R.F. Benjamin. Experimental observations of the mixing transitions in a shock-accelerated gas curtain. *Physics of Fluids*, 11(1):186–200, 1999.

[93] R.L. Holmes, G. Dimonte, B. Fryxell, M.L. Gittings, J.W. Growe, R. Schneider, D.H. Sharp, A.L. Velikovich, R.P. Weaver, and O. Zhang. Richtmyer–Meshkov instability growth: experiment, simulation and theory. *Journal of Fluid Mechanics*, 389:55–79, 1999.

[94] P. Clavin, P. Lallemand, Y. Pomeau, and G. Searby. Simulation of free boundaries in flow systems by lattice-gas models. *Journal of Fluid Mechanics*, 188:437–464, 1988.

[95] A.K. Gunstensen and D.H. Rothman. A Galilean-invariant immiscible lattice gas. *Physica D*, 47:53–63, 1991.

[96] H. Xi and G. Duncan. Lattice Boltzmann simulations of three-dimensional single droplet deformation and breakup under simple shear flow. *Physical Review E*, 59(3):3022–3026, 1999.

[97] A.P. Ershov, N.P. Satonkina, O.A. Dibirov, S.V. Tsykin, and Yu.V. Yanilkin. A study of the interaction between the components of heterogeneous explosives by the electrical-conductivity method. *Fizika Gorenia i Vzrywa (Combustion, Explosion and Shock Waves)*, 36(5):639–649, 2000.

[98] V.M. Titov, V.V. Mitrofanov, A.P. Ershov, A.L. Kupershtokh, and I.Yu. Mal'kov. Carbon in detonation processes (part B). Report done for Livermore laboratory, Institute of Hydrodynamics SB RAS, Novosibirsk, 1994. 69 p.

[99] O.N. Davydova, N.M. Kuznetsov, V.V. Lavrov, and K.K. Shvedov. On underdriven detonation in condensed he with inert ingredients. *Khimicheskaja Fizika (Chemical Physics)*, 18(4):53–66, 1999.

[100] D.I. Karpov and A.L. Kupershtokh. Models of Streamer Growth with "Physical" Time and Fractal Characteristics of Streamer Structures. In *Conference record of the 1998 IEEE Int. Symposium on Electrical Insulation*, pages 607–610, Arlington, VA, 1998.

[101] P.A. Vázquez, A.T. Pérez, A. Castellanos, and P. Atten. Dynamics of electrohydrodynamic laminar plumes: Scaling analysis and integral model. *Physics of Fluids*, 12(11):2809–2818, 2000.

[102] P.K. Watson, W.G. Chadband, and M. Sadeghzadeh-Araghi. The role of electrostatic and hydrodynamic forces in the negative-point breakdown of liquid dielectrics. *IEEE Transactions on Electrical Insulation*, 26(4):543–559, 1991.

[103] H. Yamashita, K. Yamazawa, W. Machidori, and Y.S. Wang. The effect of tip curvature on the prebreakdown density change streamer in cyclohexane. In *Proc. of the 12th Int. Conf. on Conduction and Breakdown in Dielectric Liquids*, pages 226–229, Roma, Italy, 1996. IEEE N 96CH35981.

[104] F.J. Higuera. Electrohydrodynamic flow of a dielectric liquid around a blade electrode. *Physics of Fluids*, 12(11):2732–2742, 2000.

[105] C.G. Garton and Z. Krasucki. Bubbles in insulating liquids: stability in an electric field. *Proceedings of Royal Society*, A280(1381):211–226, 1964.

[106] A. Beroual. Behaviour of charged and uncharged bubbles in dielectric liquids subjected to electric stress. *Journal of Applied Physics*, 71(3):1142–1145, 1992.

[107] S.M. Korobeinikov. The Role of Bubbles in the Electric Breakdown of Liquids: Prebreakdown Processes. *High Temperature*, 36(3):362–367, 1998.

[108] S.M. Korobeynikov, A.V. Melekhov, V.G. Posukh, V.M. Antonov, and Yu.N. Sinikh. Deformation and motion of bubbles at action of strong fields. In *Modern problems of electrophysics and electrohydrodynamics of liquids (in russian). Proc. of VI Int. Conference*, pages 187–190, Sankt-Petersburg, Russia, 2000.

[109] S.M. Korobeinikov. The Role of Bubbles in the Electric Breakdown of Liquids: Comparison with Experiment. *High Temperature*, 36(4):541–547, 1998.

[110] V. Giraud and P. Krebs. The onset of electron localization in subcritical water vapour. *Chemical Physics Letters*, 86(1):85–90, 1982.

[111] H.M. Jones and E.E. Kunhardt. Development of pulsed dielectric breakdown in liquids. *Journal of Physics D: Applied Physics*, 28(1):178–188, 1995.

[112] Z. Krasucki. Breakdown of liquid dielectrics. *Proceedings of Royal Society*, A294(1438):393–404, 1966.

[113] M. Sadeghzadeh-Araghi, M.I. Qureshi, W.G. Chadband, and P.K. Watson. Measurement of the growth of cavities and of EHD instabilities during the negative-point breakdown of silicon fluids. *IEEE Transactions on Electrical Insulation*, 26(4):663–672, 1991.

[114] V.R. Kukhta, V.V. Lopatin, and M.D. Noskov. Fractal Features of Near-Electrode Formations under Electric Discharge in Water. *Izvestija Vysshikh Uchebnykh Zavedeniy. Fizika (Russian Physics Journal)*, (7):89–92, 1994.

[115] B. Halpern and R. Gomer. Field emission in liquids. *Journal of Chemical Physics*, 51(3):1031–1047, 1969.

[116] O.A. Sinkevich and P.V. Smirnov. Heterogeneous mechanism of electrical breakdown of liquid dielectrics. *Journal of Moscow Physical Society*, 6:101, 1996.

[117] S.M. Korobeinikov. Injection Current and the Formation of Bubbles in Strong, Very Nonuniform Electric Fields. *Journal of Applied Mechanics and Technical Physics*, 41(5):831–835, 2000. (Russian edition: Prikladnaya Mekhanika i Tekhnicheskaya Fizika, pp. 75–80).

[118] P. Gournay and O. Lesaint. On the gaseous nature of positive filamentary streamers in hydrocarbon liquids. II: Propagation, growth and collapse of gaseous filaments in pentane. *Journal of Physics D: Applied Physics*, 27:2117–2127, 1994.

[119] J. Barrett and A.L. Mansell. Ultra-violet absorption spectra of the molecules H_2O, HDO and D_2O. *Nature*, 187:138–141, 1960.

[120] A.L. Kupershtokh. Investigation of non-ideal plasma generated in the channel of electric discharge in water. In *Proc. of the 15th Int. Conf. on Phenomena in Ionized Gases*, pages 345–346, Minsk, USSR, 1981.

[121] P. Bårmann, S. Kröll, and A. Sunesson. Spatially and temporally resolved electron density measurements in streamers in dielectric liquids. *Journal of Physics D: Applied Physics*, 30(5):856–863, 1997.

[122] V.V. Arsent'ev. On theory of pulse discharges in liquid. *Journal of Applied Mechanics and Technical Physics*, (5):34–37, 1965.

[123] I.Z. Okun'. Calculation of pressure acting on a piston at its constant expansion velocity. *Izv. Akad. Nauk SSSR, Mekh. Zhidk. Gaza*, (1):126–130, 1968.